Online Defect Detection for Automated Tape Layup Composite Manufacturing Processes

Colin Stewart

A thesis submitted for the degree of

***Master of Philosophy* in the**

Department of Mechanical Engineering

October 2020

Summary

It is proposed that remotely-mounted piezoelectric transducer arrays, producing and detect ultrasonic guided wave pulses, may be used to detect defects within carbon-fibre composite materials *during* their manufacture. Such arrays would provide a real-time, low-cost, way to certify materials created by automated tape layup processes without having to resort to testing procedures.

For the proposed technique to be viable,

- Pulses must be capable of penetrating the composite material and scattering from defects;
- Appropriate features must be extracted from samples which are sensitive to defects in the composite material;
- Defective materials must be distinguished from non-defective materials by an appropriate classification procedure.

The viability of the approach is examined in this thesis, by carrying out a series of physical benchtests and a series of finite element modelling simulations.

Conclusions

The conclusions of this study are summarized as follows:

1. Ultrasonic pulse energy will penetrate the composite material under manufacture and will travel preferentially along the carbon fibres, but will gradually be dissipated by the matrix material which binds the carbon fibres.

2. The detection system may be simulated with good accuracy, provided that simplifying assumptions about the actuators, the detectors, and the physical properties of the composite material can be made.

3. The ultrasonic pulses rapidly lose coherence, due to production of shear horizontal waves as they reflect from the layup surface edges. The early parts of samples gathered by detectors thus contain the most useful information and should preferentially be used to extract appropriate features.

4. The samples gathered during the physical benchtests are affected by noise and by differences in transducer transfer functions. To minimize these problems, samples need to be gathered repeatedly, and normalized appropriately.

5. It is theoretically possible to identify defects within the composite materials under manufacture, also to distinguish these defects from changes in environmental conditions, provided that a sufficiently dense array of detector transducers can be installed beneath the layup surface.

I. Background

Fibre-reinforced composite materials are commonly used create structural components for use in the aerospace, renewable industry, and automotive industries. These components are increasingly manufactured by *automated layup processes* to increase productivity and to achieve uniformity in manufactured parts.

Figure 1 illustrates the components of an automated tape placement (ATP) machine. The device consists of a *feed reel*, a *spool*, a *rolling zone*, and a *placement robot*. The feed supplies uni-directional part-cured tape ('pre-preg') to a spool which remove backing paper. A heating unit part-cures this tape and increases its adhesiveness. The heated tape is fed to the rolling zone under tension then it is applied to the layup surface by a pressure-controlled roller. The entire unit may is mounted to an industrial robot, such that tape can be laid out to create relatively complex parts which may include curved surfaces. As outlined by Lukaszewicz *et al* (2011), there has been a continuous improvement in the performance and reliability of these machines achieved over several decades. However, the machines and the tape placement robots are expensive, and as is discussed below, they cannot manufacture a flawless component.

Figure 1: ATP Manufacturing System: Key Components

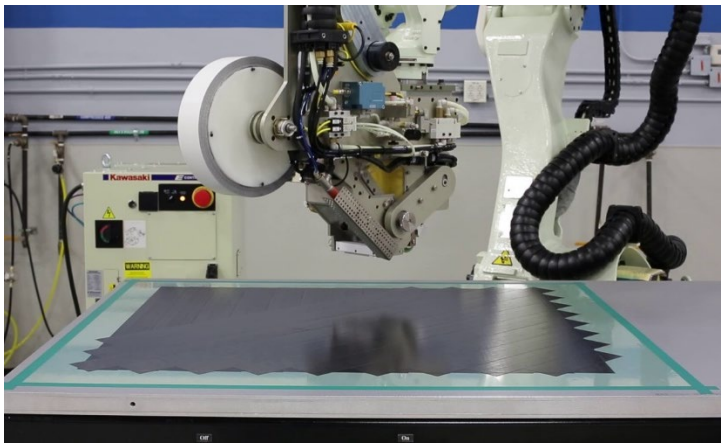

Despite the many benefits of automated manufacturing, the procedures which much be undertaken to *certify* manufactured parts for use in industry remain complex and time-consuming. The underlying cause for this complexity is the large number of failure mechanisms for fibre-matrix composite materials compared to 'conventional' (i.e. isotropic) materials. An overview of these failure mechanisms is provided by Lopes *et al* (2015). The fibres in a composite may buckle or fracture; the matrix surrounding the fibre may fracture or suffer compressive of tensile strains; or the plies may separate from each other (i.e. *delaminate*). The ultimate strength of materials is thus dependent upon uniformity of the materials on both the macroscopic and the microscopic scales.

Many imprecisions exist in the ATP manufacture process, which lead to imperfections in the manufactured composite material. These imprecisions include, for example, variations in the *feed material* (its composition and its thickness); variations in the *orientations* of the lamina which are stacked to form the final laminate, due to *imprecise control* of the layup head; changes in the *ambient temperature and* the *air moisture content*; unintended introduction of flaws such as *air bubbles*, or *tow gaps* in materials; or variations arising from deliberate introduction of *notches* or *machined holes*, which introduce stress concentrations which are

dependent on the orientations of applied loads. Each of these factors can influence all others in unforeseeable ways, and also in ways which vary depending on component geometry. The net result is that to certify a part, extremely large numbers of test coupons must be manufactured and subjected to single load tests ('certification by test'), or a smaller but still significant number of parts must be subject to complex load tests ('certification by analysis'). Feraboli (2009) presents an example of the certification procedure for a relatively simple 6-in wide load-transferring hinge component, for use in the aviation industry. This simple component required over one thousand coupon tests, or 60 full part loading tests, to achieve certification.

In summary, the strength of the manufactured materials is dependent upon how tightly manufacturing process can be controlled. Perfect control is not achievable, and therefore there will always be some flaws in materials which mean that their strength requires to be verified using complex certification procedures. These issues suggest that it would be enormously beneficial to identify flaws in composite materials at the *earliest possible stage*, i.e. *during their manufacture*, in order that certification process may be simplified, or bypassed.

1.1 Candidate Technologies

Many different types of sensing technology can be used to non-destructively test composite materials. For example, Tallman *et al* (2014) describe use of impedance tomography to measure strain distributions in carbon-fibre-polyurethane composites; Laflamme *et al* (2012) discuss use of capacitor arrays to measure strains in large civil structures; Meola & Cormigalo used infra-red thermography imaging to monitor impact damage in glass-fibre-polymer composite structures; Bull *et al* (2013) discuss the use X-ray tomography methods to identify cracks in a range of carbon-fibre composites; and Ulriksen *et al* (2017) discuss use of utap testing to measure changes in vibration modes of wind turbine rotors. A comprehensive review of these technologies, and some interesting alternatives, is provided by Gholizadeth (2016).

Though all of the technologies discussed above are capable of detecting defects in composite materials, they are oriented towards the inspection of a material *following* its manufacture. To be capable of identifying defects *during* manufacture, the sensing technology requires to be *installable* within the manufacturing arena, to be *rapid* such that data is collected while a part is being made, to have the *ability to resolve fine defects*, and finally, to have *low cost*. For carbon-fibre composite materials, these requirements are particularly well-satisfied with *ultrasonic* sensing technology.

1.2 Pulsed Ultrasonic Wave Systems

A conventional ultrasonic inspection system consists of an actuating transducer, which produces narrowband pulses of ultrasonic waves, a detector transducer, and an imaging system, as shown in Figure 2. The pulsed waves reflect and scatter from defects inside the material under inspection. When the actuator functions as the receiver, the system is known as a *pulse-echo* system. If separate transducer(s) functions as detector(s), the system is described as a *pitch-catch* system.

There are two fundamentally different ways to implement the pulsed ultrasonic wave technology. In the *normal beam inspection* (NBI) method, a pulser unit is configured to produce longitudinal waves which propagate *through* the target material as shown in Figure 2a. This pulser unit is swept over the material surface in a systematic manner to produce 'B-scan' or 'C-scan'-type images. While this NBI method can reveal fine defects in composite structures (e.g.,

Ray *et al*, 2007, and Hasaiotis *et al,* 2011), the process is time-consuming, as the volume sensed per scan is small. Furthermore, good acoustic coupling must be maintained between the pulser unit and the target material for good accuracy. It follows that this technique is *not* best suited to 'real-time' monitoring applications.

The alternative approach is the *guided wave* method, in which an actuator transducer is configured to generate guided waves, or *Lamb waves*, which propagate *across* the target material as shown in Figure 2b. These types of waves maintain an ordered structure within plate materials as they travel over long distances, whilst being strongly perturbed by defects. Thus, a single actuator and a set of detector transducers positioned at fixed locations, can efficiently sweep a large volume of a target material for defects. Moreover, when arrays of actuator and detector units are installed, arrays of actuator and detector transducers can both locate and characterize defects (e.g. Holmes *et al*, 2008 and Zhang *et al*, 2008). This type of technique is thus *ideally suited* for real time-monitoring applications.

Figure 2. Normal Beam and Guided-Wave Type Ultrasonic Inspection Technologies

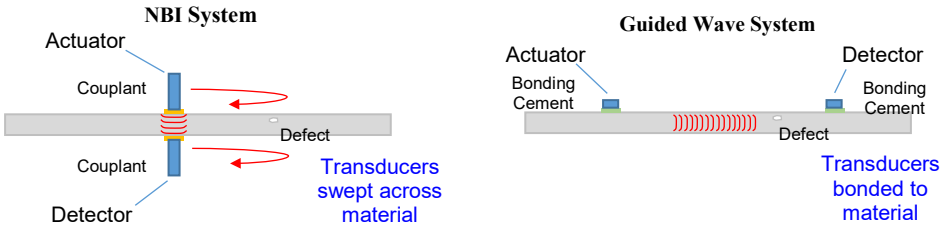

1.3 Challenges

While guided-wave type detection systems offer significant advantages over NBI-type detection systems, they also present significant challenges. These challenges may be summarized as follows:

1. The guided wave pulses must have sufficiently *short wavelengths* that they will scatter from defects within the target material.

2. The guided wave pulses must be *sufficiently intense* that samples collected by detector transducers are free from noise.

3. The samples collected by detector transducers must be processed to extract '*echo*' features, which arise because of scattering from defects.

4. The 'echo' features are sensitive to changes in *ambient temperature* and to *transfer function properties of* the individual transducers.

The feature extraction process is further complicated by *wave dispersion*, which causes guided wave pulses to 'smear out' over distance and time, and by unwanted *reflections of waves* from material boundary edges. These two effects are *mutually opposing*; that is to say, it is not possible to mitigate one effect without making the other effect more severe.

An additional challenge for an 'on-line' health monitoring application is that the ultrasonic transducers must be mounted on the tooling surface which *hosts* the manufactured part, rather than on the manufactured part itself. This means that guided waves must transfer from the

tooling surface *into* the material being manufactured, then *return into* the tooling surface for detection. However, several researchers have observed that, provided materials are well-coupled, transmission of guided waves between materials is feasible (e.g. Rohklin, 1991, Laza de Scala, 2004 and Ochoa *et al*, 2017).

II. Overview of Thesis

The objective of this thesis is to assess the ability of remotely mounted piezoelectric transducer arrays, operating in a pitch-catch mode, to detect defects within a composite part whilst it is *under manufacture*. This assessment is carried out by conducting a series of experiments which are based upon a *simplified* version of the system which is shown in Figure 3. In essence, this system is a 'snapshot in time' taken from the ATP manufacturing process, at the point where a complete sheet of material has been laid down and tape placement robot is disengaged from the tooling surface.

Figure 3: Schematic Diagram of Proposed ATP defect detection system

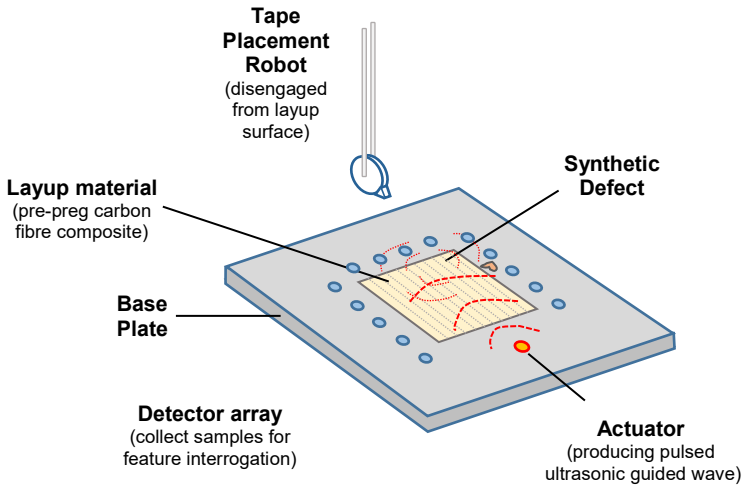

Note: Figure is illustrative only - the dimensions of base plate, the layup, and the arrangement of the transducer array are illustrative only.

Several requirements must be satisfied for the proposed technique to be viable. Firstly, the pulses produced by the actuator transducers must be able to *penetrate the layup material.* This means that transducers and layup material sheets need be *well-bonded* to the base plate, and that layup material sheets need to be *well-bonded* to each other, for viability. Secondly, pulse energy must scatter from defects sufficiently strongly that they can be distinguished by detector transducers mounted on the base plate. As discussed above, this requirement is complicated by the tendency for guided wave pulses to disperse, to reflect from plate boundaries, and also by the fact that sampled signals may be corrupted by noise. Thirdly, the defects must be distinguishable from *benign environmental changes,* such as variations in the ambient temperature, or the exact location of the layup sheet. That is to say, changes which do not affect the integrity of the material being manufactured should not trigger 'false positive' results.

The requirements for materials to be well-bonded, and for samples need to be free from excessive noise, make it beneficial to simulate the system shown in Figure 3 using *finite element software.* The simulation approach allows viability to be assessed in an *ideal* environment in which there is perfect bonding between materials, where there is no noise, and where all environmental factors can be controlled. Furthermore, a simulation approach allows an *extensive array* of transducers to be modelled at minimal cost. However, the trade-off is that it is necessary to model the system in such a way that is physically realistic while also being computationally feasible.

2.1 Thesis Structure

The main part of this thesis is split into six sections, which describe a series of physical benchtests and a series of numerical simulations. These experiments differ in several critical ways, but share common pulse actuation and data analysis techniques, which are first described in Section III. The benchtest apparatus, the scenarios tested, and the benchtests output results are described within Sections IV and V, while the numerical simulation model and simulation output results are described in Sections VI and VII. Finally in Section VIII, the results of the physical benchtests and the numerical models are compared.

III. Actuation and Data Processing Procedures

The way in which guided wave pulses are generated and the way in which the data output by detectors is processed is identical in both the physical benchtests and the numerical simulations. Therefore, it is appropriate to describe these common aspects of the experimental procedures before specific details of each experiment are discussed.

3.1 Actuation Process

In both the benchtests and the simulations, the actuator PZTs which are mounted on the base plate are driven by a modulated, sinusoidal waveform. The input to these PZT are time-varying voltages which takes the form:

$$V(t) = \begin{matrix} V_0\, sin(2\pi f_c t)\left(\frac{1}{2} - \frac{1}{2}\cos(2\pi f_e t)\right) & t \le 1/2f_e \\ 0 & t > 1/2f_e \end{matrix}$$

where f_c is a nominated carrier frequency and f_e is a nominated envelope frequency. For purpose of this study the carrier frequency f_c is chosen as 280 kHz. This value is based on the results of preliminary physical benchtests, performed using the selected PZT transducers (SONOX-P5 type), in order to investigate frequency which produced highest signal-to-noise output ratio in the experimental data. Particularly strong output signals were observed at the chosen 280kHz frequency, which are attributed to high mode excitability and electro-mechanical resonances within the transducers.

The envelope frequency is set to f_e= 14kHz (i.e. $f_e = f_c/20$). This frequency produces a burst of twenty carrier cycles over a duration of 71μs, as is shown in Figure 4. The selection of the envelope frequency is driven by the conflicting requirements that f_e should be low, such that the actuation frequency spectrum is narrow, but should also be reasonably large to keep the excitation burst short, such that defects can be easily distinguished from the carrier burst and from reflections at plate boundaries. Ultimately, there is no 'right' or 'wrong' answer to this decision; it is a choice made to minimize two conflicting problems.

Figure 4: Actuation Waveform, Benchtests and Numerical Simulations

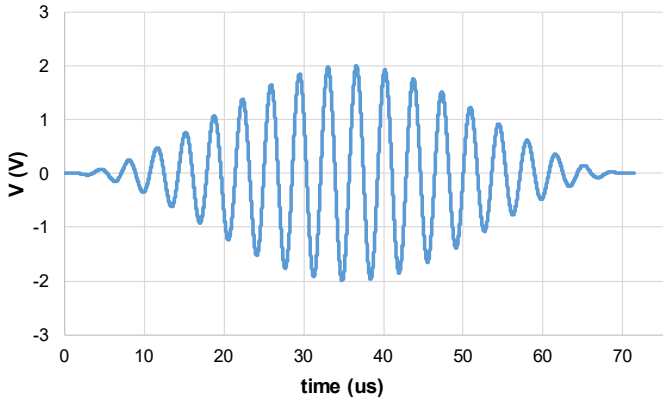

Figure 5 illustrates the actuation waveform frequency spectrum and the phase velocities for S- and A- mode Lamb waves in a 10mm aluminium plate (as used in the physical benchtests) and in a 4mm aluminium plate (as used in the numerical simulations). Within the 4mm plate, the actuation pulse induces weakly-dispersive S_0 and A_0 modes. Within the 10mm plate, must faster-travelling, more highly-dispersive, S_1 and A_1 wave modes may also be induced. The

exact *amounts* of each wave mode depends upon the physical properties of the actuating transducer, and how tightly, and uniformly the transducer is bonded to the base material. In general, these factors cannot be completely controlled.

When the actuation transducer is circular in shape, the wave modes travel as *circular-crested Lamb waves*. These modes decay with distance travelled from the actuator. An analytical solution for these types of waves travelling in an *unbounded* plate, under condition of *perfect bonding,* exists, which is attached in Appendix A for reference. This solution is useful for checking experimental output, and for checking the accuracy of numerical simulations.

Figure 5: Lamb wave phase velocities for d = 4 mm and d = 10 mm aluminium plates. The actuation waveform spectrum is superimposed for comparison.

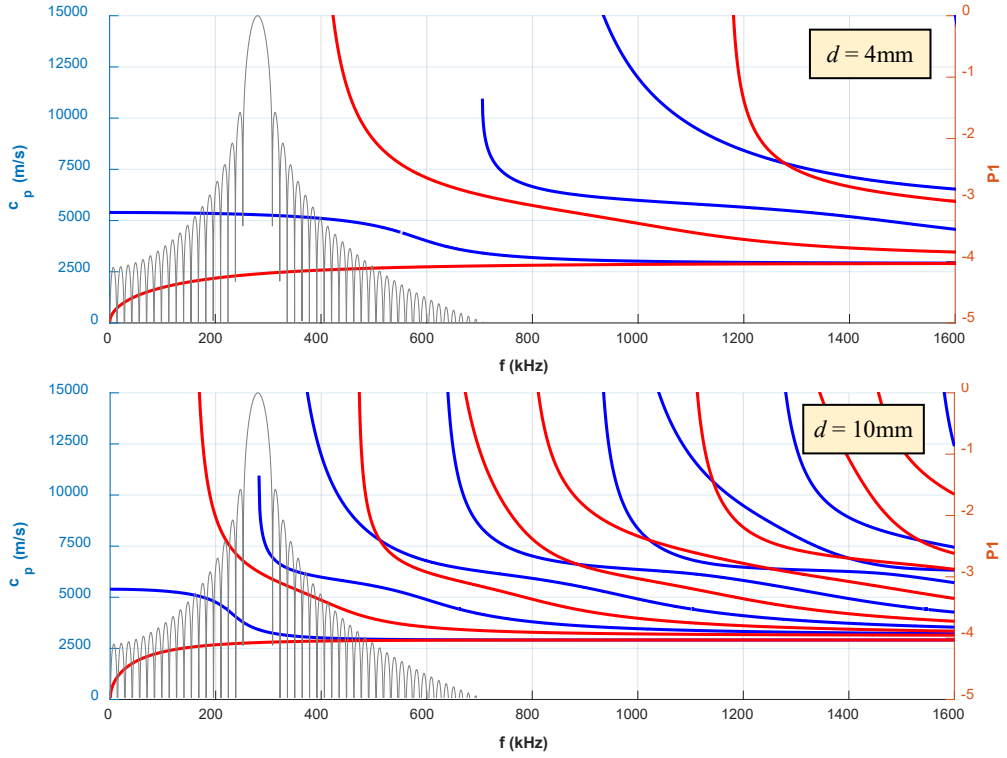

3.2 Output Data

The physical benchtests and the numerical experiments produce $n_t \times n_d$ matrices of output data which shall be denoted as $\boldsymbol{U}$. The parameter n_d is the number of detectors in each measurement system, and parameter n_t is the number of time-series data points gathered by each detector. The values of n_t and n_d which apply to the benchtests and the simulations, and are summarized in Table 1, alongside the sampling intervals, Δt, and the duration of samples, t. It is noted that while that n_t is large in the physical benchtests (reflecting the fact that it is easy to collect long-duration samples), n_d is relatively large in the numerical experiments (reflecting the fact that it is easy to simulate large numbers of detectors).

Multiple sets of experiments are performed in which the number of plies of layup material, the sizes and shapes of artificial defects, and so on, are varied. To distinguish between individual experiments, a set of state parameters 'X', is appended to the each output data matrix within *bracketed subscripts*, as a shorthand, thus: $\boldsymbol{U}_{\{X\}}$. The items contained in this set 'X' have

different labels, and these labels have different meanings for the physical benchtests and the numerical simulations. Details are provided in Table 2 which follows and are discussed further in the relevant sections below.

Note that the data gathered during benchtests are subject to *experimental noise*, and hence they are *samples* taken from a probability distribution $\boldsymbol{U}$. As shown, a set of $n_s = 40$ samples from $\boldsymbol{U}$ are gathered.

Table 1: Physical Benchtests and Numerical Simulations: Dimensionality of Output Data

	Sampling Period	**Total Sample Duration**	**No. Samples**	**No. Detectors**	**No. Time Series Points**
	$\boldsymbol{\Delta t}$	$\boldsymbol{t}$	$\boldsymbol{n_s}$	$\boldsymbol{n_d}$	$\boldsymbol{n_t}$
Physical Benchtests	25 ns	20 ms	40	28	800×10^3
Finite Element Simulations	10 ns	200 µs	-	841	2×10^3

Table 2. Physical Benchtests and Finite Element Simulations: Experiment Identifier Labels

Physical Benchtests	**Finite Element Simulations**
$\boldsymbol{U}_{\{t,\,p,\,i\}}$ Test number (1, 2, 3) Layup ply number (0, 1, 2, 3) Sample index number* *(optional)* (1 - 40)	$\boldsymbol{U}_{\{m,\,a,\,b\}}$ Layup material type (0, I, II) Change Imposed on Layup (1)* *(optional)* (D1, D2, D3, P1, P2, P3) Change Imposed on Layup (2)* *(optional)* (D1, D2, D3, P1, P2, P3)

3.3 Feature Extraction

The collected sets of measurements, $\boldsymbol{U}$, require to be processed such that will reveal, and ideally locate, defects within the carbon-fibre layup material. This data manipulation process is summarized in Figure 5. The general idea is that two experimental measurements, $\boldsymbol{U}_{\{a\}}$ and $\boldsymbol{U}_{\{b\}}$, are used to extract two lower-dimensionality features $\boldsymbol{t}_{\{a\}}$ and $\boldsymbol{t}_{\{b\}}$, and then to evaluate a single *change feature*, $\Delta\boldsymbol{t}_{\{b\}\{a\}} = \boldsymbol{t}_{\{b\}} - \boldsymbol{t}_{\{a\}}$. Typically, $\boldsymbol{U}_{\{a\}}$ is obtained from an experiment where a defect is present in the layup, while $\boldsymbol{U}_{\{b\}}$ is obtained from an experiment where a defect is *not* present in the layup. The change feature $\Delta\boldsymbol{t}_{\{b\}\{a\}}$

In deciding *how* the features should be extracted from the output data, three issues are here taken into consideration. Firstly, it is unfeasible to run numerical simulations of guided waves for extended periods of time, since simulations are computationally expensive (and they may eventually lose accuracy, due to numerical diffusion). Secondly, the guided waves *lose coherency* as they are reflected from plate boundaries, since on each reflection, they are

subjected to mode conversions (Santhanam & Demirli, 2013)[1]. This effect would suggest that *the earliest parts* of data samples will convey the most useful information, and that should preferentially be used for feature extraction. Thirdly, there is a desire to keep the feature extraction process as *simple as possible*. Based on these issues, features are extracted from sample data using a threshold level algorithm, which indicates the *time-of-arrival of the first meaningful information* at each transducer in the transducer array.

Guided wave pulses produce oscillating signals, so in order to implement a threshold level algorithm, data require to be *prepared.* This preparation process is illustrated in Figure 6. The measured data $\boldsymbol{U}$ are first normalized, to produce the matrix $\boldsymbol{U}^n$ then envelopes of the time-series vectors $\boldsymbol{U}^n$ are extracted; in this study, this extraction is performed by *convoluting the time-series data* using a nominated function $\boldsymbol{\psi}$. Denoting the i^{th} time-series vector of the matrix $\boldsymbol{U}^n$ as $\boldsymbol{u}_i$, the resulting i^{th} output vector of $\boldsymbol{Y}$, $\boldsymbol{y}_i$, is given by:

$$\boldsymbol{y}_i = \boldsymbol{u}_i * \boldsymbol{\psi} = \sum_{j=1}^{j=n_t} \boldsymbol{u}_i[j]\boldsymbol{\psi}[j' - j]$$

where $\boldsymbol{\psi}$ is the discretized version of a nominated function, ψ. The choice of function ψ is arbitrary; for the purpose of this study ψ is selected to a Morlet wavelet:

$$\psi(t) = \sqrt{\pi f_b}\ e^{\,2\pi i f_c t}\ e^{-t^2/f_b}$$

as proposed by Fuentes *et al* (2017). The carrier frequency f_c is 280 kHz, while the parameter f_b is given the nominated value $f_b = 1.5/f_c^2$ (units s^{-2}). This produces the wavelet which is shown in Figure 7a.

Figure 7b shows an example of the output vector $\boldsymbol{y}$ which is obtained from a typical input vector $\boldsymbol{u}$. As the basis function $\psi(t)$ is complex, $\boldsymbol{y}$ is contains amplitude *and* phase information. The phase of $\boldsymbol{y}$ conveys information about arrival of the different Lamb wave modes and/or the reflections of pulses from any sharp edges or plate boundaries, and while this information may be useful, it is not considered further here. The modulus, or the *envelope*, denoted by $|\boldsymbol{y}|$, is used as the input for feature extraction.

The threshold level algorithm requires a nominated threshold parameter, θ, to be supplied as input. This parameter permits a $1 \times n_d$ vector of data, , to be extracted from $|\boldsymbol{Y}|$, where the j^{th} entry of this vector is the first time point which satisfies the relation:

$$t_j = t_{(|\boldsymbol{y_i}| > \theta)}$$

As shall be discussed in Sections 5 and 7 below, the parameter θ needs to be carefully chosen such that the output vector $\boldsymbol{t}$ conveys useful information. Furthermore, it should be noted that as the data contained in $|\boldsymbol{Y}|$ are discrete, i.e. they exist only for the Δt intervals which are shown in Table 1, the algorithm has *limited precision*. This precision is not sufficient for the analysis which follows, and therefore, the dimensionality of the $|\boldsymbol{y_i}|$ vectors is first increased using a cubic spline interpolation algorithm functioning with a time interval of 1 ns. Thus, the entries in $\boldsymbol{t}$ have a precision of ± 0.5ns.

It should be noted that, while the feature vectors obtained from numerical simulations are deterministic, in the physical benchtests each vector $\boldsymbol{t}$ is a sample from a probability distribution $\boldsymbol{t}$. As indicated by Table 1, sets of 40 samples from $\boldsymbol{t}$ are drawn.

[1] This subject is discussed in further detail in Section 7.1 below.

Figure 6: Defect Detection Process

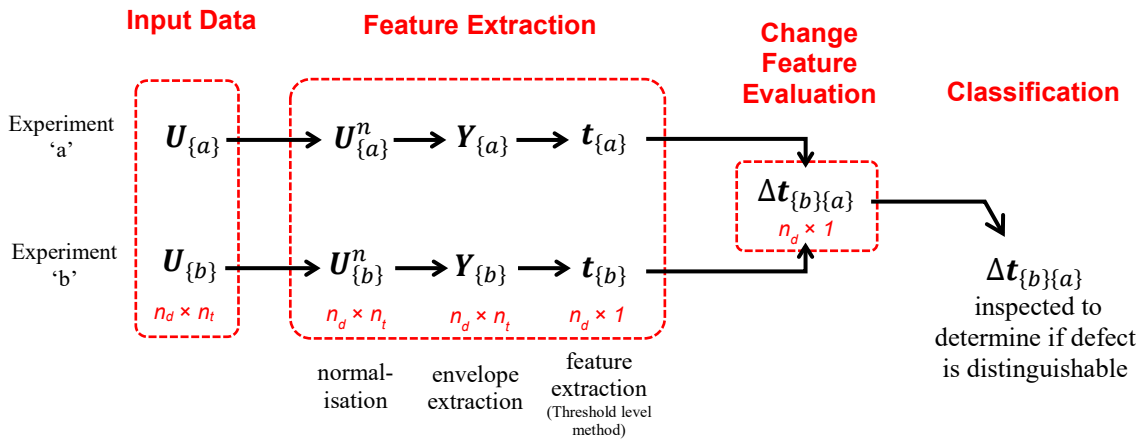

Figure 7: Signal convolution: basis function $\psi(t)$ and resultant outputs $\phi(t)$ and $|y(t)|$for a typical input $v(t)$

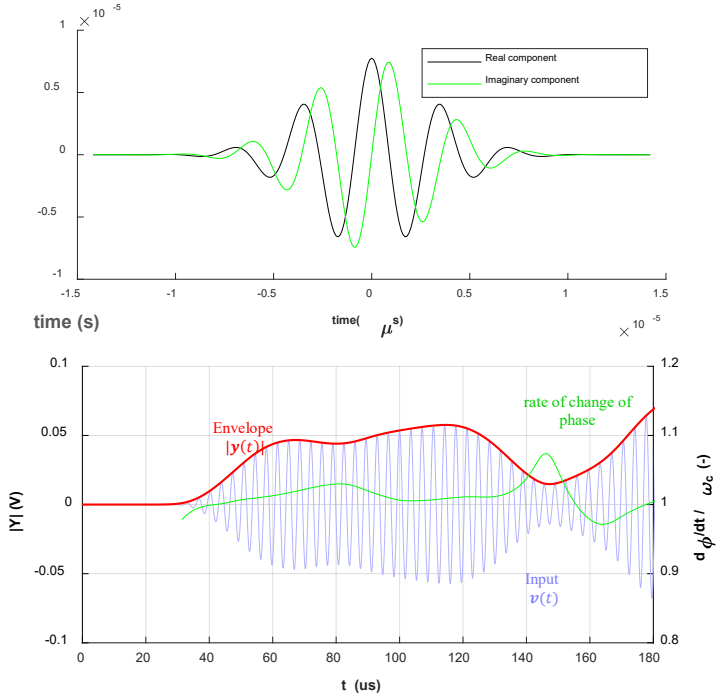

IV. Physical Benchtests

Physical benchtests are performed using the apparatus which is shown in Figure 8. This apparatus comprises an aluminum base plate, a layup zone which hosts sheets of part-cured pre-preg carbon fibre composite material, and a group of eight 10mm diameter Sonox-P5 type PZT transducers, bonded to the base plate using epoxy cement. The transducers are arranged as four closely-spaced pairs (Aa/Ab, Ba/Bb, Ca/Cb and Da/Db). The first four transducers (Aa, Ab, Ba, Bb) function as actuators *and* detectors, while the remaining four transducers (Ca, Cb, Da, Db) function solely as detectors.

A series of three tests are performed with the apparatus, which are detailed in Table 3. In east test, sheets of uni-directional of pre-preg material, cut to dimensions of 200 × 200 × 0.25 mm, are manually pressure-rolled onto the layup surface, with their lower corner placed at the reference point with their carbon fibres aligned normal to the y-axis. Prior to the layup of the first ply, and then following layup of each ply, a series of samples are gathered. Each actuator transducer (Aa,Ab,Ba,Bb) is selected in turn. This selected actuator transducer is excited 40 times, at 1 second intervals, applying the waveform shown in Figure 4. Samples are collected from the seven remaining transducers at 25 ns sampling intervals, for a duration of 20ms; the first 4ms portion of these 20ms samples *precede* each actuation. When this process is carried out over the four actuators, the output is a $n_d \times n_t = (4 \times 7) \times 800 \times 10^3$ matrix, which is denoted as $\boldsymbol{U}$. The samples are pre-filtered using a 4th-order bandpass filter shown in Figure 9, to remove unwanted noise and 50Hz mains components.

Table 3 indicates that, in each test, four plies are pressure-rolled onto the layup surface. The test number, the ply number, and the sample numbers are distinguished by indices appended in subscripts to the matrix $\boldsymbol{U}$. In Tests 1 and Test 2, there are no defects, such that Test 2 offers a repeatability check for Test 1. In Test 3, an artificial defect is introduced between plies 2 and 3, taking the form of a circular dual-layered Teflon sheet located to the upper right of the layup as shown in Figure 10a. An infra-red thermographic image of this defect, taken once covered by the ply is shown in Figure 10b. The defect is clearly visible.

It is convenient to assign *transducer pair indices* to each of the $n_d = 28$ actuator-detector pairs which are used to gather samples, for purpose of analysis which follows. These indices are summarized in Table 5. The locations of the transducers, and the symmetry of the base plate, means that several *groupings* of transducer pairs can be identified. These grouping are given the labels which are shown by Table 5.

It is also important to note the factors which have potential to impact on the measured samples, and subsequent features. Firstly, the three experimental three tests were performed on *consecutive days*, with ambient room temperatures for each test recorded in Table 4. As a result, there is an *ambient temperature variation* of 3°C between tests. Furthermore, since the pre-preg sheets have been cut and placed manually, there may be subtle variations in the *sizes* of each layup sheet, the *position* at which each ply is placed relative to the reference point shown in Figure 8, the *orientations* of the carbon fibres relative to the y-axis shown in Figure 8, as well as the way in which each ply is *bonded* to its underlying surface. In the analysis that follows, these effects will be collectively described by using the term '*ply placement variations'*. In contrast to the variation in room temperature, these effects cannot be properly quantified.

The challenge in the experimental tests is thus to distinguish the defect from benign effects of ambient temperature variation, and also ply placement variation, in the presence of

experimental noise. These issues shall be discussed in the course of the results section which follows.

Figure 8: Physical Benchtests: Apparatus

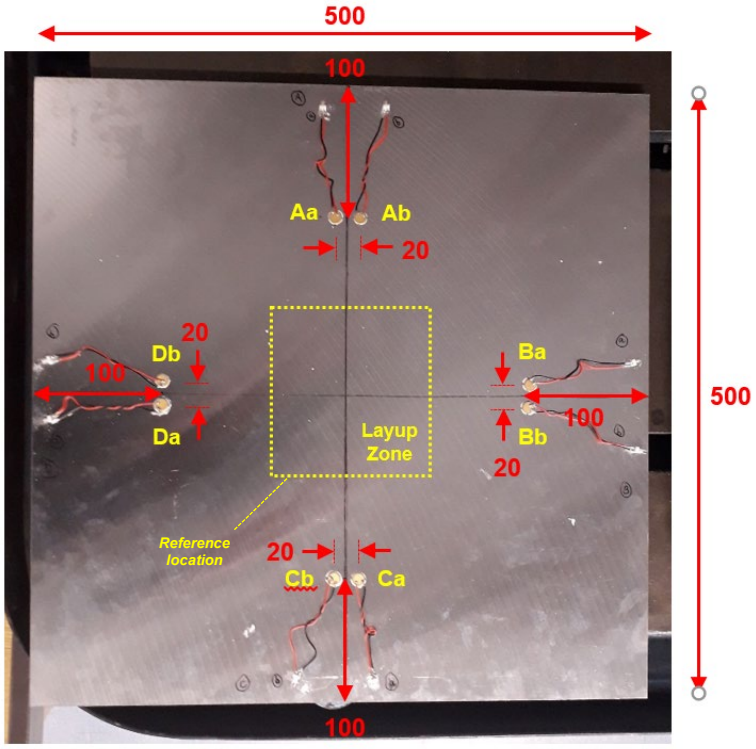

	Dimensions	Material
Base Plate	500×500×4	Aluminium
Layup (each ply)	200×200×0.25	Carbon-Fibre Pre-Preg

Table 3: Physical Benchtests: Case Summary Table

Case Description	No. Layup Plies	Defects	Ambient Temp-erature	No. Cases	Output
Test 1 ('Base Case')	4 $p \in \{0,1,2,3,4\}$	-	20°C	200 (40 × 5)	$\boldsymbol{U}_{\{1,p,i\}}$
Test 2 ('Repeatability Case'	4 $p \in \{0,1,2,3,4\}$	-	17°C	200 (40 × 5)	$\boldsymbol{U}_{\{2,p,i\}}$
'Test 3' (Defect Case)	4 $p \in \{0,1,2,3,4\}$	Single defect between Ply2 and Ply 3*	20°C	200 (40 × 5)	$\boldsymbol{U}_{\{3,p,i\}}$

Note: Circular dual-layer Teflon sheet with r=13mm, location co-ordinates (in mm): (155,45)*

Table 4: Physical Benchtests: Transducer Pair Indices (n_d)

		Detector							
		Aa	**Ab**	**Ba**	**Bb**	**Ca**	**Cb**	**Da**	**Db**
Actuator	Aa	-	*2**	3	4	5	6	7	8
	Ab	-	*10**	11	12	13	14	15	16
	Ba	17	18	-	*20**	21	22	23	24
	Bb	25	26	-	*28**	29	30	31	32

*Note: Actuator and detector are adjacent. These pairs do not yield useful information about composite material, so data are not used.

Table 5: Physical Benchtests: Transducer Pair Groupings

Label	No. of groups	No. pairs in group	Detector Pair Indices	Details
"Neighbor-Actuator Duos"	12	2	{3,11} {4,12} {5,13} {6,14} {7,15} {8,16} {17,25} {18,26} {21,29} {22,30} {23,31} {24,32}	Pairs of transducer pairs which have same actuators, but have neighbor detectors.
"Neighbor-Detector Duos"	12	2	{3, 4} {5,6} {7,8} {11,12} {13,14} {15,16} {17,18} {21,22} {23,24} {25,26} {29,30} {31,32}	Pairs of transducer pairs which have neighbor actuators, but have same detectors.
"Mirror Image Duos"	4	2	{3,17} {4,25} {11,18} {12,26}	Pairs of transducers pairs where actuator and detector are swapped.
"Single Actuator Group"	4	6	{3 - 8} {11 - 16} {17, 18, 21-24} {25, 26, 29-32}	Groups of transducer pairs which share same actuator.
"Neighbor Actuator Groups"	2	2 × 6	{3 - 8} & {11 - 16} {17, 18, 21-24} & {25, 26, 29-32}	Pairs of "single actuator groups" having neighbor actuators.
"Through Ply Pairs"	2	4	{5, 6, 13, 14} (normal) (23, 24, 31 32} (perpendicular)	Transducer pairs aligned on opposite sides of layup separated by c.30cm; carbon fibres are aligned near-normally or near-perpendicularly to the transducer axis.
"Cross Ply Pairs"	1	16	{3, 4 ,7, 8, 11, 12, 15, 16, 17, 18, 21, 22, 25, 26 29 ,30}	Transducer pairs aligned on adjacent sides of layup separated by c. 22 cm; carbon fibres aligned obliquely to transducer axis, at approximately 45 degrees.

Figure 9: Sampling bandpass filter transfer function

(Yellow line as shown).

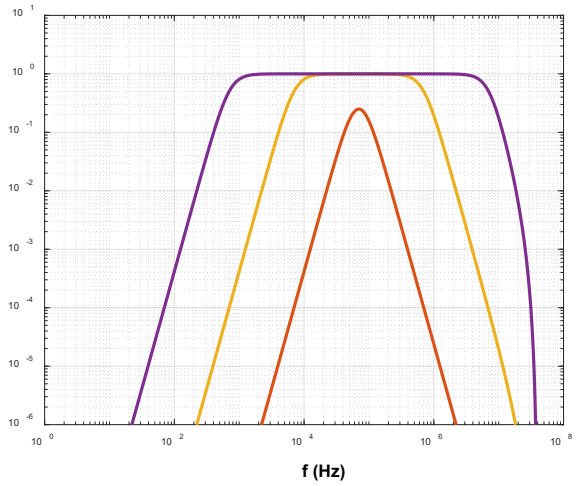

Figure 10: Artificial defect. Introduced between Ply 2 and Ply 3 During Test 3

Photo

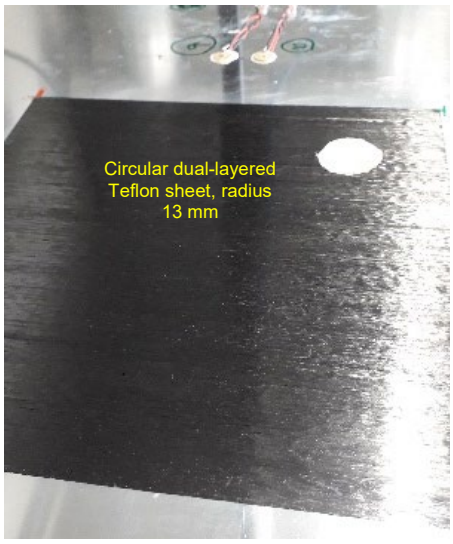

Infra-red thermograph, obtained following layup of Plies 3 and 4.

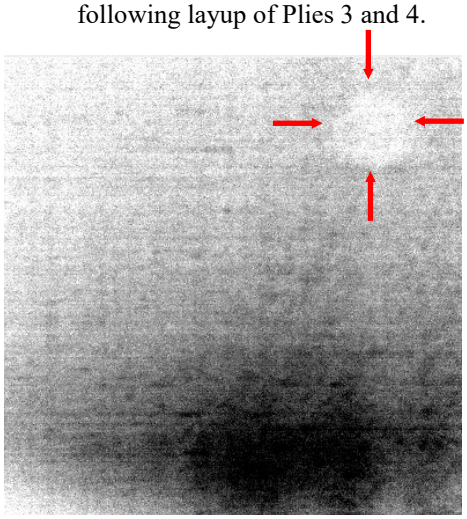

V. Physical Benchtest Results

In this section, results from the benchtests are discussed. This discussion is split into five subsections, with Sections 5.1 to 5.3 focusing upon *output samples*. Section 5.1 discusses general properties of samples obtained from a single transducer pair. Section 5.2 discusses, in greater detail, properties of the initial parts of these samples which are considered to hold most relevant information. Section 5.3 compares the samples obtained from groups of transducer pairs, and discusses how these groups of samples may be normalized.

The following three subsections focus upon the *features* which are derived from output samples using the threshold level algorithm. Section 5.4 discusses the *general properties* of features, while Section 5.5 discusses the *changes* in features, which may occur as a result of (e.g.) laying down pre-preg sheets. Finally Section 5.6 presents summary statistics which may be used to compare features against analogous features which are obtained from the numerical experiments (described in Section 7).

5.1. General Properties of Samples

Figures 11a, 11b and 11c illustrate typical samples which are collected from Tests 1 and Test 3, with *none*, *one*, *two* and *three* plies placed on to the base plate. These samples obtained from the transducer pair with index $n_d = 3$ (i.e. actuator Aa and detector Ba). Note that in Test 3, the artificial defect shown in Figure 8 is inserted between Ply 2 and Ply 3.

Figure 11a shows the amplitude of the *raw output voltage data*, upon on a log scale[2]. The oscillations detected by the detector transducer peak around 100μs after the actuation commences, then maintain a plateau level for a short period, then decay exponentially to a background level.

Figure 11b shows the *cumulative energy* $E(t)$ of this voltage data on a log scale, as defined by the function:

$$E(t) = \int_0^t |U(t')|^2 dt'$$

This figure illustrates, correspondingly, that the cumulative energy rise rapidly, but reaches a plateau value by the end of the 16ms sampling period. These plateau values become progressively *lower*, as more ply layers are laid down upon the base plate. Hence, the results indicate that the pre-preg composite material is rapidly absorbing the mechanical energy being input to the base plate by the actuator.

Figure 9c shows the *frequency spectra* of the raw output data. All of the spectra have a dominant band centred at the carrier frequency (280kHz). All of the spectra also contain secondary peaks, but these peaks are far smaller than the dominant band, and appear to be unrelated to the carrier frequency.

There is nothing obvious within Figures 11a, 11b, 11c to suggest the presence of the inter-ply defect introduced between plies 2 and 3 in Test 3[3]. This is perhaps to be expected, as the guided wave field rapidly becomes *incoherent* as it reflects over and over again from the base plate boundaries and on each reflection, it is subject to mode conversions and to production of shear horizontal waves. It is also equally possible that the defect has been rendered invisible due to slight changes in ambient room temperature between the tests and variations in the way that

[2] Transducer output data are first bandpass filtered using the filter shown in Figure 8.

[3] This conclusion is reached when data from other transducer pairs are analyzed and also when individual samples in the set of $n_s = 40$ measurement are analyzed.

plies have been rolled onto the base plate. The sections that follow therefore focus upon the changes which arise due to the layup of the *first ply only*, and which take place over an *initial period* where the field is coherent. For purpose of discussion that follows, this term 'initial period' refers to the first 150μs of the output data.

Figure 11: Typical output samples u, obtained from Tests 1 and 3 for Transducer Pair with index $n_d = 3$.

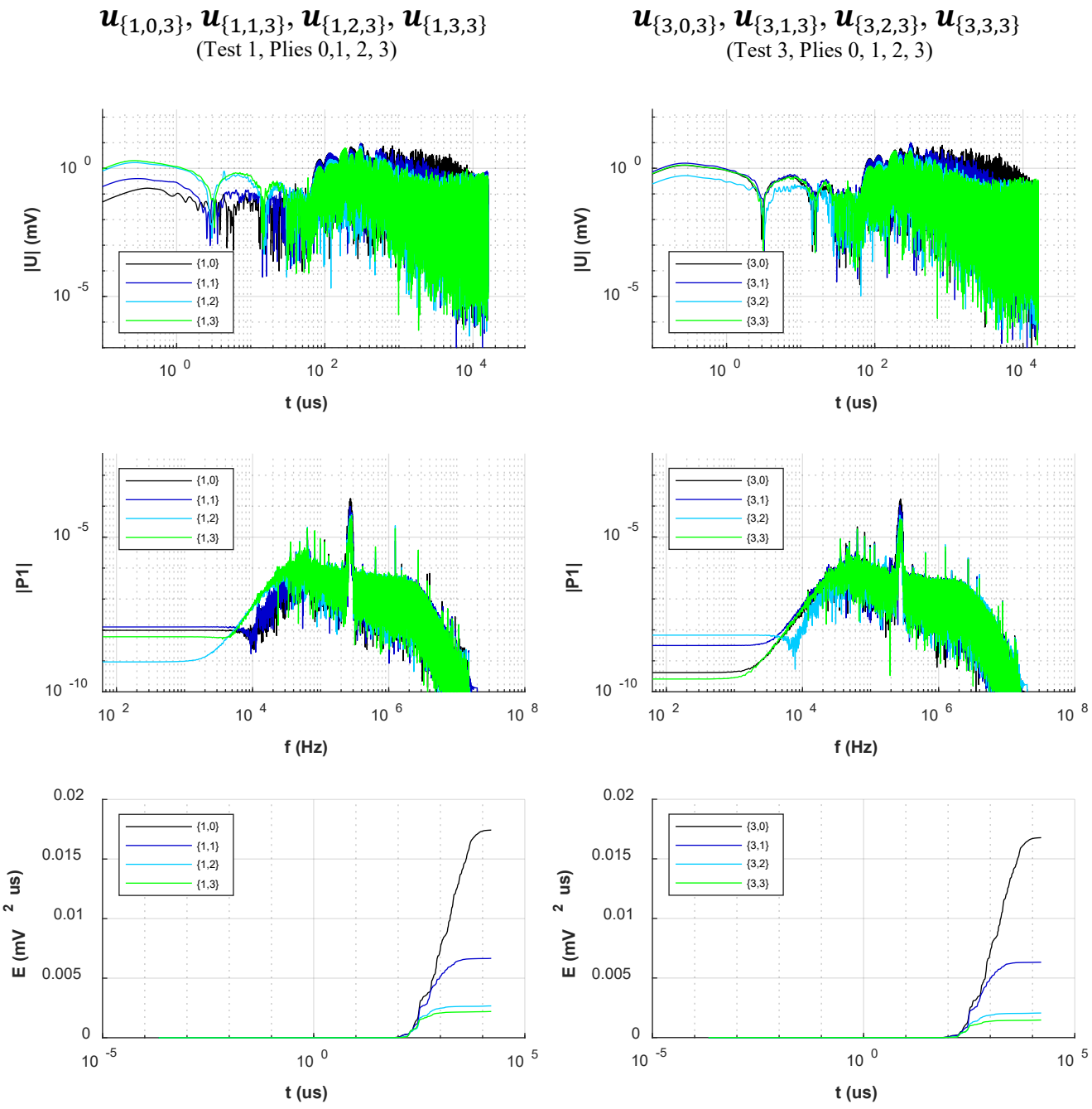

5.2. Output Data from a Single Transducer Pair

Figure 12 illustrates the initial 140 µs period of the 40 samples of data obtained from detector pair $n_d = 3$, $\boldsymbol{U}_{3\{1,0\}}$ (obtained during Test 1, with no layup). The mean sample value $\overline{\boldsymbol{U}}_{3\{1,0\}}$ is illustrated by the black line. For this particular transducer pair, a fast-travelling S_0 mode arrives after approximately 70µs, followed by a slower-travelling and partially-superimposed A_0 wave mode at approximately 90 µs. The times-of-arrival are in rough agreement with the analytic solutions for surface disturbances occurring due to S_0 and A_0 wave modes propagating in a 10mm unbounded plate, shown in Figure 13.

The root-mean-square noise level, which can be estimated by evaluating the integral $\left(\frac{1}{T}\int (U-\bar{U})^2\, dt\right)^{0.5}$, is approximately 50µV.

Figure 14 shows the frequency spectra of the *residuals*, $\boldsymbol{U}-\overline{\boldsymbol{U}}$, which are obtained from the 1 ms segments of the detector data which are *immediately prior* to each actuation (i.e. the 1ms segments which are collected 999ms *after* each preceding actuation). The mean value of these frequency spectra is illustrated by the black line. The spectrum contains several prominent peaks, most notably at 63kHz. The graph shows that the noise is not truly Gaussian, but is dominated by residual vibrations at the natural frequencies of the base plate.

Figure 15 shows the set of $\boldsymbol{Y}_{3\{1,0\}}$ envelope features which are obtained by convolution $\boldsymbol{U}_{3\{1,0\}}$, (plotted first on a linear scale and then a log scale). The mean feature $\overline{\boldsymbol{Y}}_{3\{1,0\}}$ is indicated by the black line. The figure shows that also evidence of a *disturbance* prior to the arrival of the S_0 mode. This disturbance is strongly correlated with the actuation waveform, suggesting that samples are affected by *crosstalk*, that is to say, *capacitive leakage* of the actuator input waveform through the system.

Figure 12: Set of 40 samples $\boldsymbol{U}_{3\{1,0\}}$, and mean value $\overline{\boldsymbol{U}}_{3\{1,0\}}$ (black line)

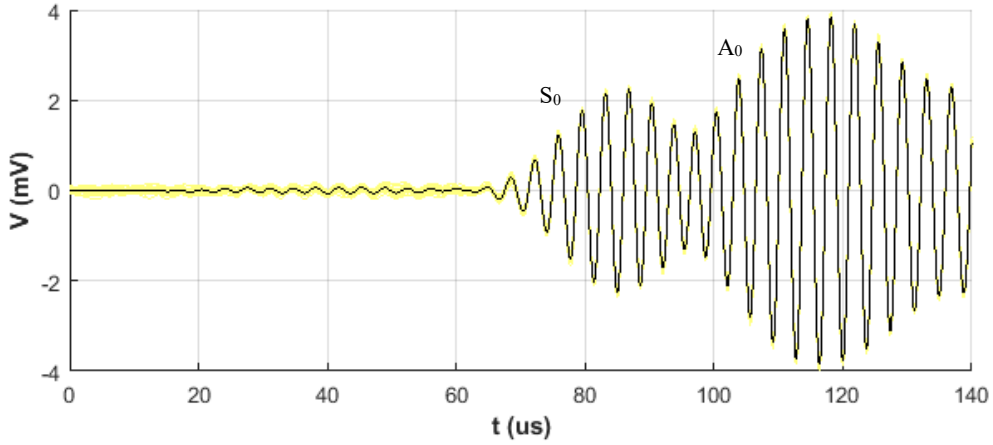

Figure 13: Analytic Solution: – h = 10mm unbounded plate – ideal PZT actuator, separation distance r = 20cm

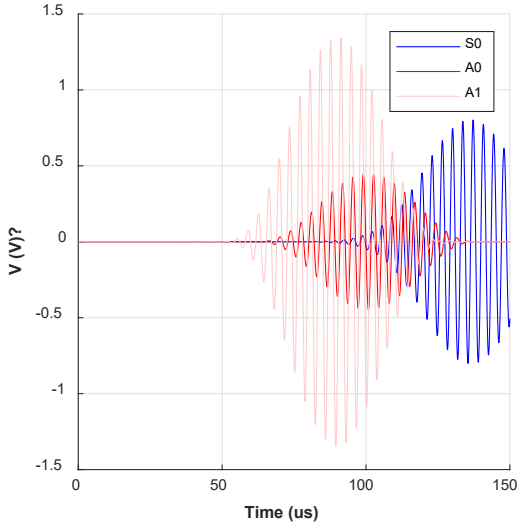

Figure 14: Frequency spectra of residuals $\boldsymbol{U}_{3\{1,0\}}$- $\overline{\boldsymbol{U}}_{3\{1,0\}}$ (obtained from 1ms segment of data, 999ms after each action)

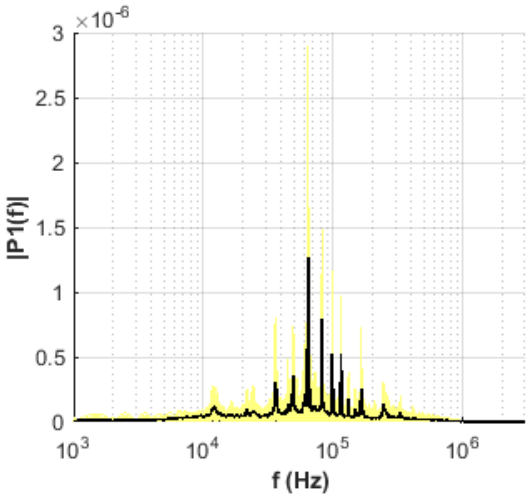

Figure 15: Set of $\boldsymbol{Y}$ features and mean feature $\overline{\boldsymbol{Y}}$. (a). Linear Scale. Figure (b). Log Scale.

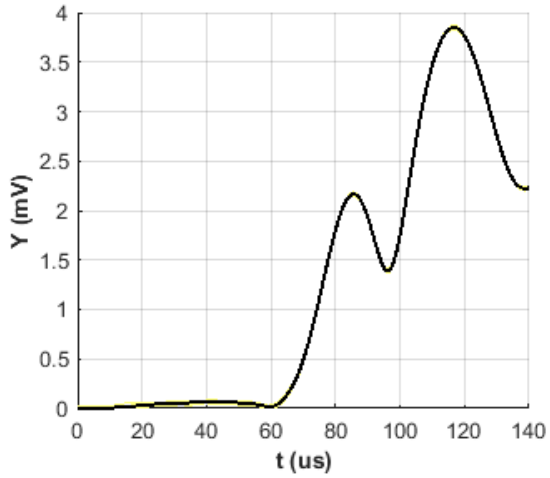

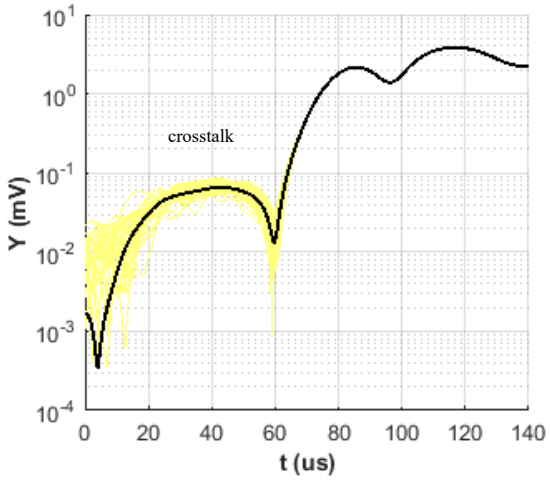

5.3. Convoluted Output Data

Figures 16a, 16b and 16c, compares the convoluted data, $\overline{\boldsymbol{Y}}_{\{1,0\}}$, obtained from a *single actuator transducer set*, from two *neigbour-actuator transducer pairs groups*, and from two *mirror image transducer pair groups*. (These groups are defined in Table 5 above). The data shown are mean values, obtained by averaging over 40 samples taken from Test 1 when there is no layup. Data are shown on linear and logarithmic scales.

The $\overline{\boldsymbol{Y}}$ features within the 'single actuator set' (Figure 16a) are noticeably different from each other, as might be expected given the differences in transducer separation distances, r. The $\overline{\boldsymbol{Y}}$ features within the 'neighbor actuator' groups are more similar; and this similarity is

particularly evident when the data are viewed on the logarithmic scale (Figure 16b). The $\overline{\boldsymbol{Y}}$ features within the 'mirror image' groups are particularly similar when viewed on a logarithmic scale; but despite the pairs in this group having identical separation distances, *r*, the features are not identical (Figure 16c). Moreover, the leading edges of *all* features, associated with the arrival of S_0 wave modes, rise at different rates.

The difference between the features shown in Figure 16 may be explained as a combination of several effects. Firstly, there may be some natural variation in piezoelectric material contained *within* each of in the transducers. Secondly, there may be variations in the *bonding layers* which bind each PZT transducer to the base plate, which will affect the way in which electrical signals are converted to mechanical motions and vice versa. Thirdly, transducers may be affected by *electromechanical resonance* to varying levels; this resonance which may significantly amplify, or attenuate, mechanical motions. Finally, there is the possibility that the bonding layers cause scattering of waves as they arrive at detecting transducers, leading to different levels of distortion on detected signals. The combined impact of these phenomena is clearly substantial and it is not controllable. It is also worth pointing out that even very subtle shifts in the arrival times of the S_0 and A_0 modes at detectors have a significant impact on the convoluted output signal, Y. This effect may be appreciated by examining Figure 9, in which three individual modes have been isolated.

To minimize the variations that such effects have upon the $\boldsymbol{Y}$ features, data are *normalized* using the cumulative energy function $E(t)$. The normalized feature for the i^{th} transducer pair is given by the expression:

$$\boldsymbol{y}_i^n = \alpha_i \boldsymbol{y}_i = \frac{\boldsymbol{y}_i}{\beta\sqrt{E_i^e}}$$

where each α_i is a normalization factor (units V^{-1}). This factor is defined by the overall *accumulated sample energies*, E_i^e ($E_i^e = \int_0^\infty Y(t)^2\, dt$, units V^2 s) and a *normalization constant* β (units $s^{1/2}$). The value of β is chosen such that the maximum amplitude of the normalized features in the set of n_d transducer pairs features is unity.

Figures 17 and 18 show cumulative energy functions, E^e , and normalized data $\overline{\boldsymbol{Y}}^n_{\{1,0\}}$ for the single actuator transducer set 'Aa'. The normalized data shown in Figure 14a have more consistent leading edges than the samples shown in Figure 12a, which lends them more amenable to feature extraction.

Figure 16a: Convoluted data $Y_{\{1,0\}}$ for a 'single actuator set' (Actuator Aa, n_d = {3-8})

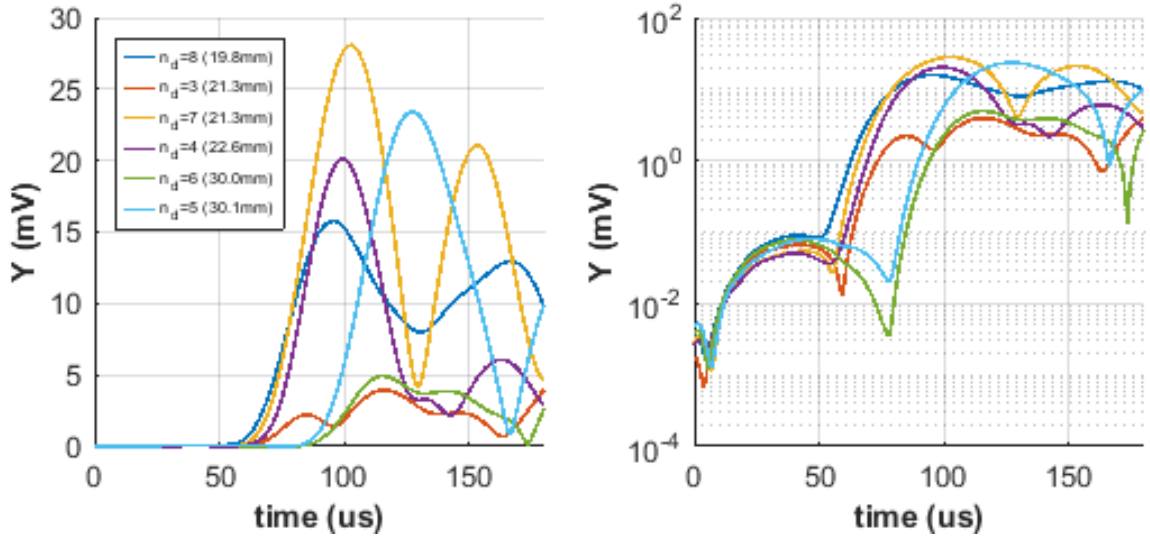

Figure 16b: Convoluted data $Y_{\{1,0\}}$ for two 'neighbour actuator' pairs (n_d = {3, 11} & {7, 15})

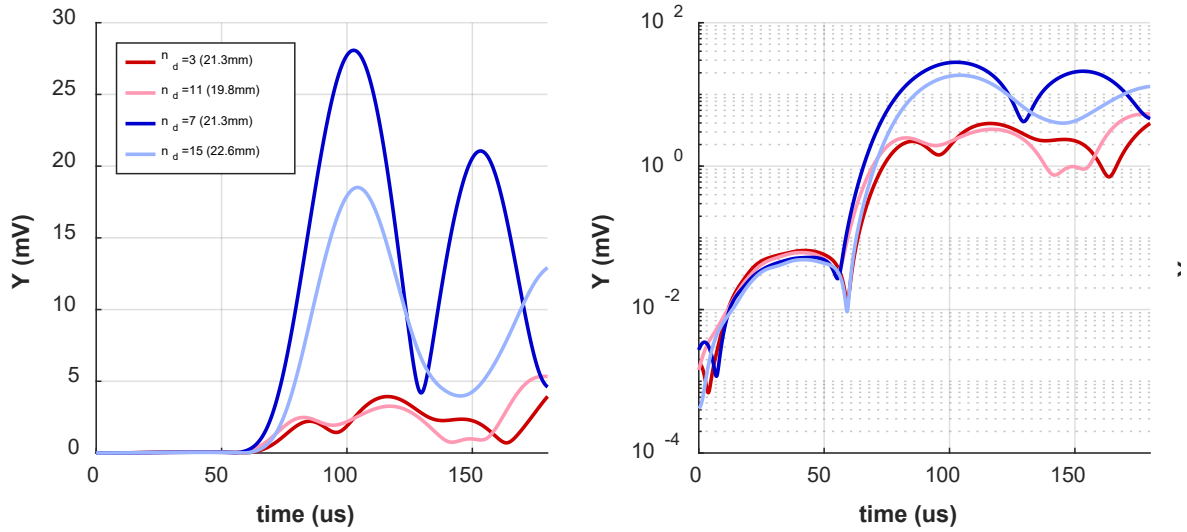

Figure 16c: Convoluted data $Y_{\{1,0\}}$ for two 'mirror image' pairs (n_d = {3, 17} & {12, 26})

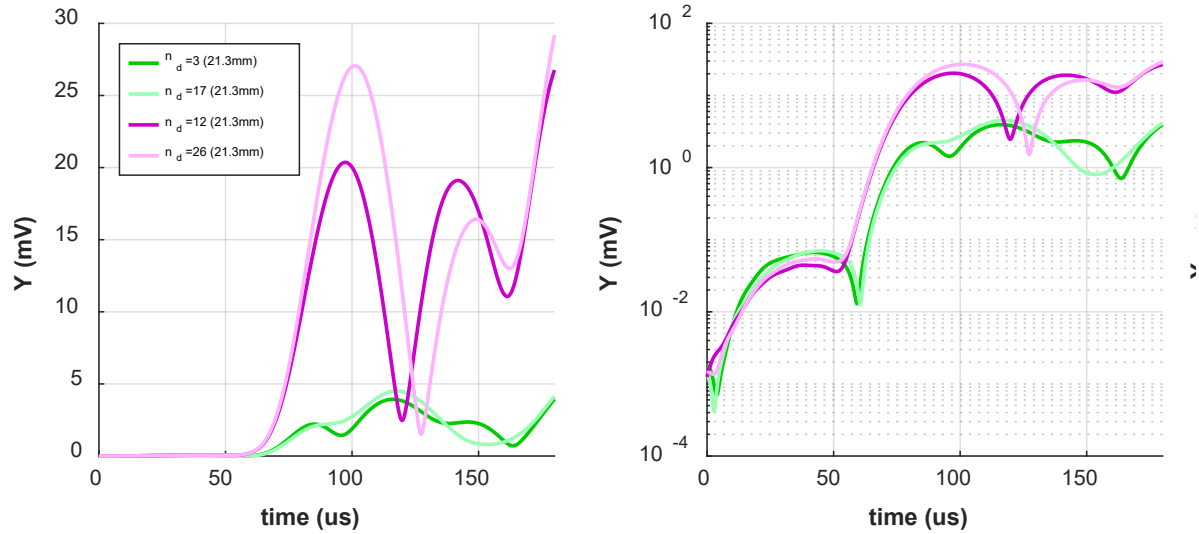

Figure 17: Cumulative Energy $E_{\{1,0\}}$, for 'single actuator set' Aa

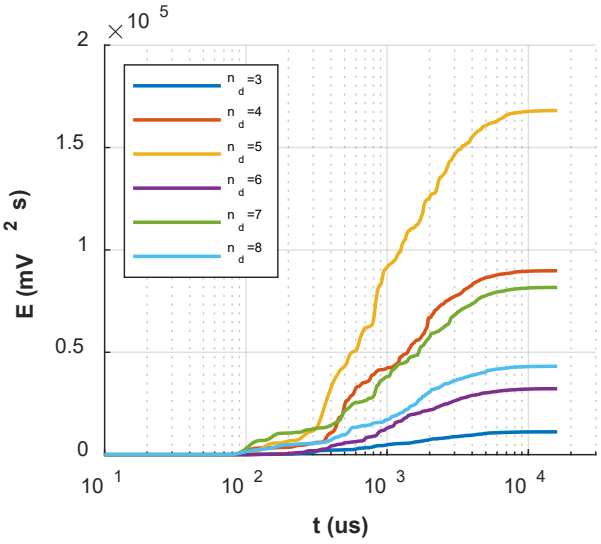

Figure 18: Normalized Convoluted features $Y^n_{\{1,0\}}$ for 'single actuator set Aa'

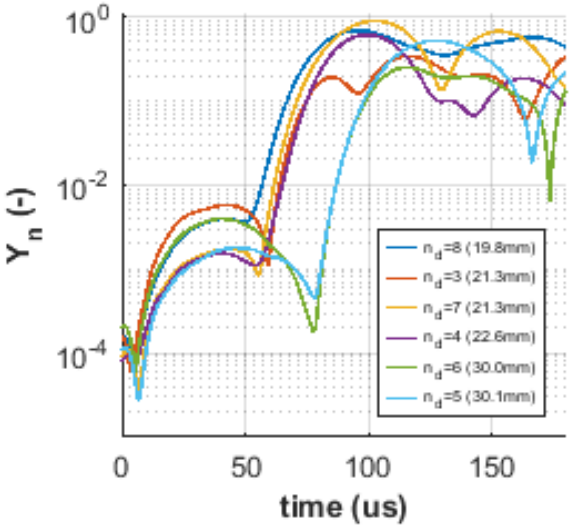

5.4 Feature Analysis

The output features, $\boldsymbol{t}$, are extracted from the normalized samples, $\boldsymbol{Y}_n$, using a threshold level algorithm. Inspection of Figure 18 suggests that the threshold level parameter θ should be set in a range $\theta = 0.01$ - 0.10, in order that this algorithm to return typical arrival times for S_0 mode wave groups reaching each detector. If θ is set above this range, the algorithm occasionally triggers on the slower A_0 mode in preference to the S_0 mode; if setting θ below this limit causes algorithm will trigger on the crosstalk and the noise which precede the relevant part of each sample.

Figure 19 illustrates *mean* feature values, $\bar{\boldsymbol{t}}_{\{1,0\}}$, which are obtained for Test 1 when there is no layup material (nominated values $\theta = 0.01$ and $\theta = 0.10$). Results are plotted a function of actuator-detector pair separation distances, r. The theoretical *arrival times*, *peak disturbance* times, and *termination times* for S_0 mode wave groups propagating in the 10mm thick base plate are superimposed as dotted lines. (These lines assume that the actuation pulse lasts 71µs, as shown in Figure 2, and assume (reasonably) that the S_0 wave mode is minimally dispersive). The values in $\bar{\boldsymbol{t}}$ lie very close to the theoretical arrival times lines, particularly when the lower threshold value is applied ($\theta = 0.01$). This result agrees with expectations.

Figure 19 also illustrates *standard deviations* in feature values, $\sigma_{\boldsymbol{t}\{1,0\}}$. The results are plotted as a function of the normalizing parameter α. The figures indicate that the lower the threshold level, θ, or the higher the normalization parameter, α, the greater the uncertainty in t due to the effects of crosstalk and signal noise. In other words, to minimize the uncertainty in t, the threshold level parameter θ should be set as *high as possible* and *'strong' signals should be selected in preference to 'weak' signals.*

The group of eight feature entries defined by indices $n_d = \{3, 11, 17, 18, 21, 22, 23, 24\}$, which are highlighted in Figure 19 by a dotted red line boundary, have been obtained using the PZT transducer Ba as the actuator or the detector. It is evident that the feature entries set produce

have particularly large standard deviations. These results suggest that transducer Ba is *anomalous* is some way - there is something is affecting the amplitude of the signals which are produced or detected, relative to other transducers, and which is causing particularly large uncertainty in features. While the exact cause of the anomaly is not known, this set of features is *discarded* in some of the analysis which follows.

Figure 19: Mean feature values, $\bar{t}$, and standard deviation of mean feature values, $\sigma_{t\{1,0\}}$, with no layup present (Test 1, θ=0.01 and θ=0.10)

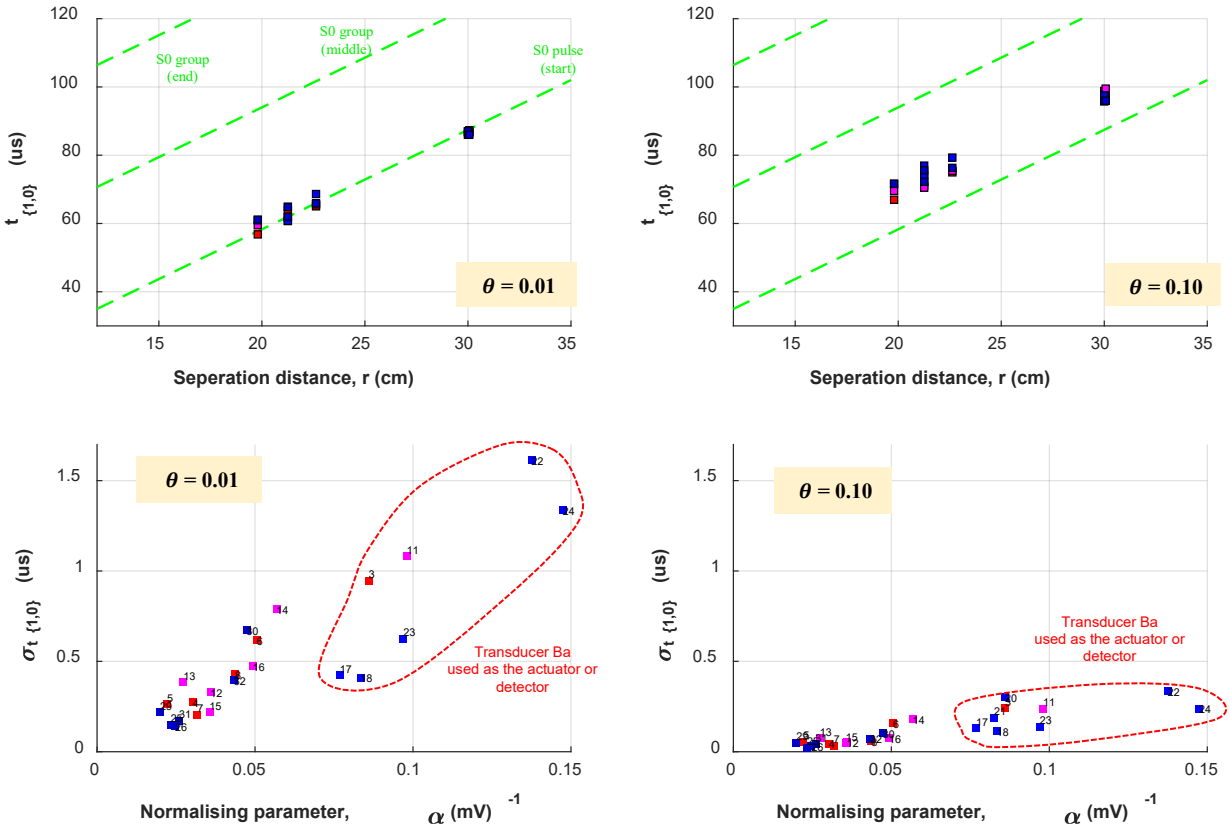

5.5. Change Feature Analysis

Figures 20a, 20b and 20c present changes in $\boldsymbol{t}$ features, $\Delta\boldsymbol{t}$, which can be derived by comparing the $\boldsymbol{t}$ features obtained from the no ply ($p = 0$) and the single ply ($p = 1$) tests. The figures show, respectively, changes which occur *within each test following layup of a single ply*; changes which occur *between tests prior to layup*, and changes which occur *between tests following layup of a single ply*. Each graph shows changes in mean feature values $\Delta\bar{\boldsymbol{t}}$ and standard deviations of these feature values $\sigma_{\Delta\boldsymbol{t}}$, plotted as a function of transducer pair index n_d. The data are produced using the threshold level parameter $\theta = 0.01$ and the standard deviations are estimated from sample data using a bootstrapping technique. The actuating transducers Aa/Ab/Ba/Bb are highlighted on each figure. The 'through-ply' changes are indicated using square-shaped markers, while the 'cross-ply' changes are indicated using diamond-shaped markers[4].

[4] Refer to Table 5 which shows the transducer pairs in each of these groups.

The changes which occur due to layup of a single ply, illustrated in Figure 20a, are denoted as $\Delta\boldsymbol{t}_{\{1,1\}\{1,0\}}$ $\Delta\boldsymbol{t}_{\{2,1\}\{2,0\}}$ and $\Delta\boldsymbol{t}_{\{3,1\}\{3,0\}}$. All entries in these three features are *positive*, indicating that the placement of the layup material has *delayed* the arrival of the actuator wave pulse at the detectors. However the *orientations* of the carbon fibres relative to the transducer pair axes have significant effect on this time delay. The largest components in $\Delta\boldsymbol{t}$, of the order of 2 μs, are obtained from the through-ply pairs whose detectors are aligned *perpendicularly* to the carbon fibres (n_d = {23, 24, 31, 32}). Smaller $\Delta\boldsymbol{t}$ components, of the order of 0.5-1.0 μs, are obtained from the through-ply pairs whose detectors are aligned *parallel* to the fibres (n_d = {5, 6, 13, 14}). For cross-ply pairs, where detectors are aligned *obliquely* to the fibres, small changes in the lengths of layup material lying in the paths between the actuator and transducer have a significant effect on $\Delta\boldsymbol{t}$. These results indicate that wave energy preferentially travels *through* the carbon fibres.

If the data are separated according the various geometry groups which are defined by Table 5, several other trends can be observed. The features obtained from the twelve data *neighbor-detector* duos ({i_d, i_d+1}, where i_d is odd), are closely correlated, as would be expected. The features obtained from the *neighbor-actuator* pair sets ({Aa, Ab} and {Ba, Bb}) are also closely correlated, as would be expected. Finally, the features which are obtained from the four *mirror-image duos* ({3,17},{4,25},{11,18},{12,26}) are particularly closely correlated, but they are *not identical*.

The changes which occur between tests prior to layup, illustrated in Figure 20b, are denoted as $\Delta\boldsymbol{t}_{\{2,0\}\{1,0\}}$, $\Delta\boldsymbol{t}_{\{3,0\}\{2,0\}}$ and $\Delta\boldsymbol{t}_{\{1,0\}\{3,0\}}$. These changes may be attributed to the *variation in ambient temperature* which was observed between tests. These $\Delta\boldsymbol{t}$ features are significantly smaller than the features shown in Figure 18a. Furthermore, there is a tendency for the components in $\Delta\boldsymbol{t}_{\{2,0\}\{1,0\}}$ to be negative, and for the components in $\Delta\boldsymbol{t}_{\{3,0\}\{2,0\}}$ to be positive. These trends appear to be consistent with the recorded temperatures, on the basis that the base plate might expand slightly when ambient temperature increases and contract slightly when ambient temperature decreases.

If the data are separated into to the *neighbor-detector*, *neighbor-actuator*, and *mirror-image* groups, as per the analysis above, similar trends are observed. The data in these sets are closely correlated, especially so for the mirror-image duos. However, the data from the set of pairs which involving transducer Ba (n_d = {3, 11, 17, 18, 21, 22, 23, 24}), as either the actuator or the detector transducer, are notable outliers. As discussed in Section 5.4, there is evidence that this transducer may be anomalous. The data obtained from this transducer shall be thus discarded, in summary analysis which follows.

The changes which occur between tests following layup of a single ply, illustrated in Figure 20c, are denoted as $\Delta\boldsymbol{t}_{\{2,1\}\{1,1\}} - \Delta\boldsymbol{t}_{\{2,0\}\{1,0\}}$, $\Delta\boldsymbol{t}_{\{3,1\}\{2,1\}} - \Delta\boldsymbol{t}_{\{3,0\}\{2,0\}}$, and $\Delta\boldsymbol{t}_{\{1,1\}\{3,1\}} - \Delta\boldsymbol{t}_{\{1,0\}\{3,0\}}$. These changes are attributed to the variation in the placement of plies between the tests, under the assumption that the impact of the ambient temperature is linearly separable[5]. The components of $\Delta\boldsymbol{t}$ are considerably *smaller* than shown in Figure 20b, but they are *larger* than shown in Figure 18a. Some of the components are positive, indicating that in some locations the placement variation has *delayed* the arrival of the wave pulse, whereas other components are negative, indicating that in some locations the placement variation has *accelerated* the arrival of the wave pulse. Some of the components are particularly large (e.g. for the pairs n_d = 25 and n_d = 31), suggesting that there might be a trapped bubble near to

[5] This assumption appears to be reasonable, on the basis of the results of numerical simulations which are discussed in in Section VII.

transducers Da and Db. Once again, the *neighbor-detector*, *neighbor-actuator*, and *mirror-image* groups of pairs in Figure 20c are closely correlated, and, the data obtained from the group involving the transducer Ba appear to be anomalous.

In contrast to Figures 20a and Figures 20b, the *underlying causes* of the change features which are shown in Figure 20c remain unknown. A larger and denser detector transducer array would be beneficial, as this would perhaps allow any anomalies which are present in the bonding layer to be located.

Figure 20(a). Changes in t features during each test, due to layup of a single ply ($\theta = 0.1$)

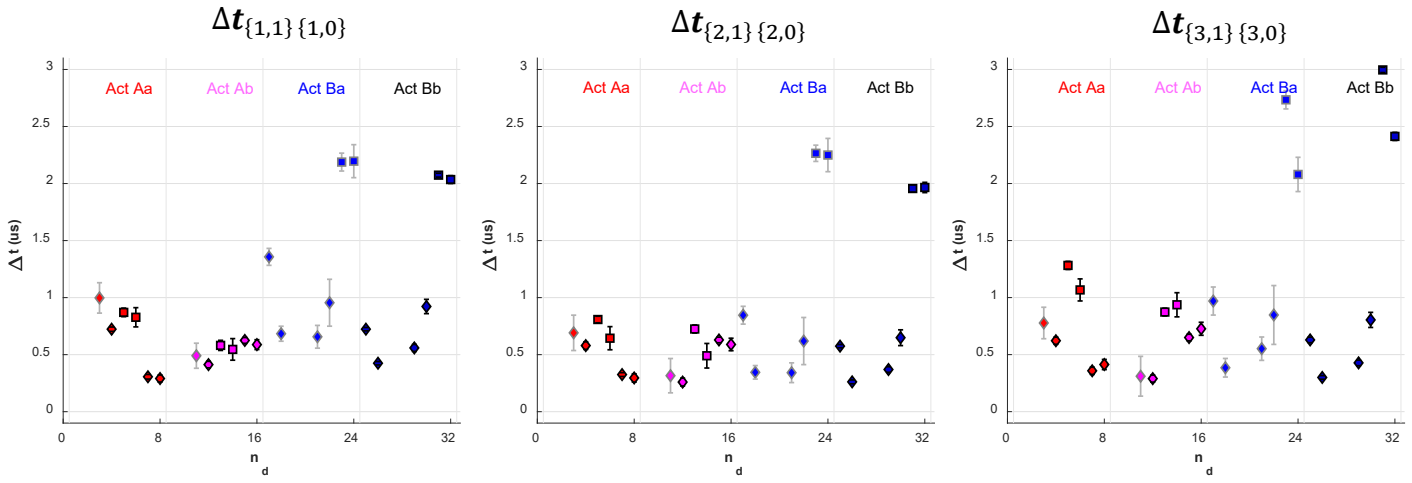

Figure 20(b). Changes in t features between tests, with no ply layup ($\theta = 0.1$)

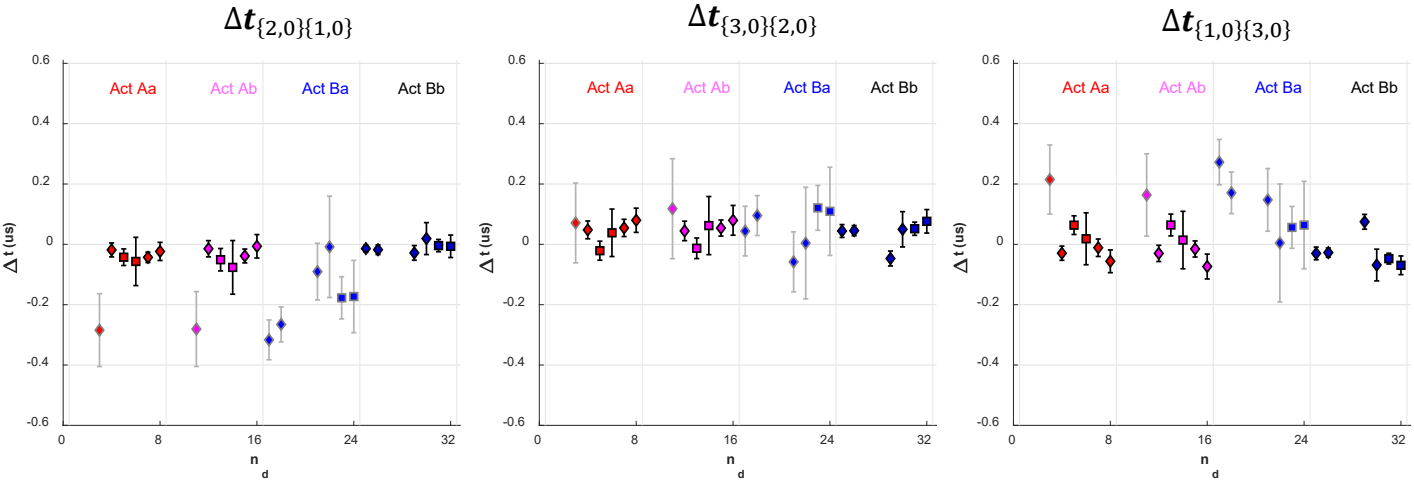

Figure 20(c). Changes in single-ply layup Δt features between tests, with background features from Figure 14(b) removed ($\theta = 0.1$).

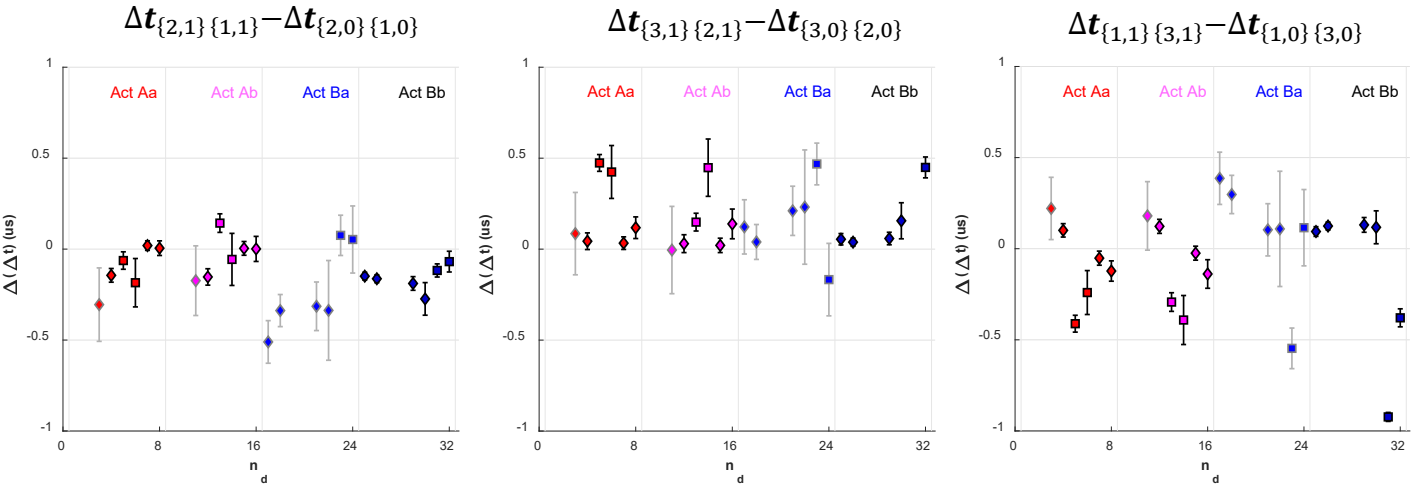

5.6 Summary Statistics

It is convenient to reduce the change features shown in Figures 20a, 20b and 20c to *summary statistics*, such that features obtained from the benchtests can be directly compared against features obtained from modelling simulations (which are presented in Section 7.5 which follows).

Table 6 presents summary statistic values μ, for the *layup of a single ply*, for a *change in the ambient temperature*, and for the group of effects being collectively described as the *ply placement variations*. The calculation methods used to derive each statistic, and groups of transducer pairs used in evaluations, are indicated for reference. It is noted that, while the ply layup and ambient temperature changes Δt features which have a *definite* polarity, the ply placement variation produce Δt features which *do not have definite* polarity. Therefore, statistics $\bar{\mu}_a$, $\bar{\mu}_b$ and $\bar{\mu}_c$ are based upon mean values, but statistic $\bar{\mu}_d$ has been based upon a variance value.

The statistics which are shown on the right-hand side of the table are intended to give rough estimates of changes in the features, t, which arise from the changes shown. It is noted that, in the case of the $\bar{\mu}_d$ summary statistics, the underlying cause of the change which produces this statistic remains unknown. It is also emphasized that as data are obtained from a limited number of tests, and that some of the basis data are not independent, the summary values shown on the right are *crude estimates*.

Table 6: Summary change statistics for *ply layup*, *ambient temperature variation* and *ply placement variation*

Change		Calculation method	Averaging group	Summary Statistic Value
Layup of Single Ply	Transducer pairs *normal* to fibres	$\mu = \frac{1}{\lvert S\rvert}\sum \Delta t_n$ $\bar{\mu}_a = \frac{1}{3}\sum \mu_i$	{23, 24, 25, 26}	$\bar{\mu}_{a1}$ = 804 ns
	Transducer pairs *parallel* to fibres	$\mu = \frac{1}{\lvert S\rvert}\sum \Delta t_n$ $\bar{\mu}_b = \frac{1}{3}\sum \mu_i$	{5, 6, 13, 14}	$\bar{\mu}_{a2}$ = 2162 ns
Ambient Temperature Variation		$\mu = \frac{1}{\lvert S\rvert}\sum \Delta t_n$ $\bar{\mu}_c$ is the gradient of the straight line fitting the (μ_i, ΔT) data pairs	{4-8, 12-16, 25-26, 29-32}[1]	$\bar{\mu}_b$ = 18 ns/°C
Ply Placement Variation		$\sigma = \frac{1}{\lvert S\rvert}\sqrt{\sum \Delta t_n^2}$ $\bar{\mu}_d = \frac{1}{3}\sum \sigma_i$	{4-8, 12-16, 25-26, 29-32}[1]	$\bar{\mu}_c$ = 223 ns

Note 1: The data from transducer pairs n_d = {3, 11, 17, 18, 21, 22, 23, 24}, are omitted from these calculations, on the basis that the 'Ba' transducer may be anomalous. Refer to Figure 17 above.

VI. Numerical Simulations

Numerical simulations are performed using the model of the system which is shown in Figure 21. As with the physical benchtests, this system comprises of an aluminum base plate and a layup zone which hosts layers of uni-directional composite material. The dimensions of the base plate and the layup material differ from the dimensions of the physical system, for reasons which shall be discussed below. The system has a *single* actuator, of diameter d = 10 mm. The system also has an *extensive array* of detectors which cover the *rear face* of the base plate at regular 1cm intervals as indicated by the grid lines.

Table 7 illustrates the numerical simulation case list. Initial reference cases are performed without a layup, and then with a non-defective layup. Series of simulations are then performed where changes are imposed upon the layup material. Three of these imposed changes are *simulated defects*, and three of these imposed changes are *environmental changes*. The environmental upsets affect the output data, but they are not critical to the manufacture process. In the first series of cases, a single change is imposed on the layup. A second series of cases is performed in which two changes are imposed on the layup material.

During each simulation, the actuator is excited by the 280kHz carrier burst which is shown in Figure 4. Output signals are sampled from 29 × 29 array of virtual detectors at 10ns sampling intervals, for a total duration of 200μs. The entire output from each simulation is thus a $n_d \times n_t$ = 841 × 2001 matrix, which is denoted as $\boldsymbol{U}$. The individual detector output in $\boldsymbol{U}$ are identified by the expression $n_d = 29(i_y - 1) + i_x$ (i.e. units are numbered in rows, from bottom-left to top-right, with the actuator located above the detector having n_d = 711). The terms shown in Table 7, which are appended to $\boldsymbol{U}$ in brackets subscripts, are used to distinguish each of the simulation cases.

The simulations produce output data which are free from the interference, from the noise, and from the variations in the PZT transducer functions which have been shown to affect the output data of physical benchtests. As such, they provide the opportunity to interrogate the output data in an *idealized* environment. Furthermore, the regular array of virtual detectors units allows the output features to be turned into images, which (as shall be seen) are extremely beneficial when analyzing the results. However, prior to these discussions, the details of the simulation model are presented. A number of practical issues require to be overcome, which concern the model dimensions, the meshing strategy, the modelling of the materials, the way in which PZT actuators and detectors are simulated, and how the defects are modelled and meshed. These issues are also discussed in depth.

6.1 Model Dimensions

As shown in Figure 21, the simulated base plate has dimensions 300 × 300 × 4.0 mm, and the composite layup plies each have dimensions 120 × 120 × 0.5 mm. Thus, the base plate is considerably smaller and thinner than, and the layup plies are considerably smaller and thicker than, their benchtests equivalents.

Figure 21: Numerical Simulations: Model Schematic

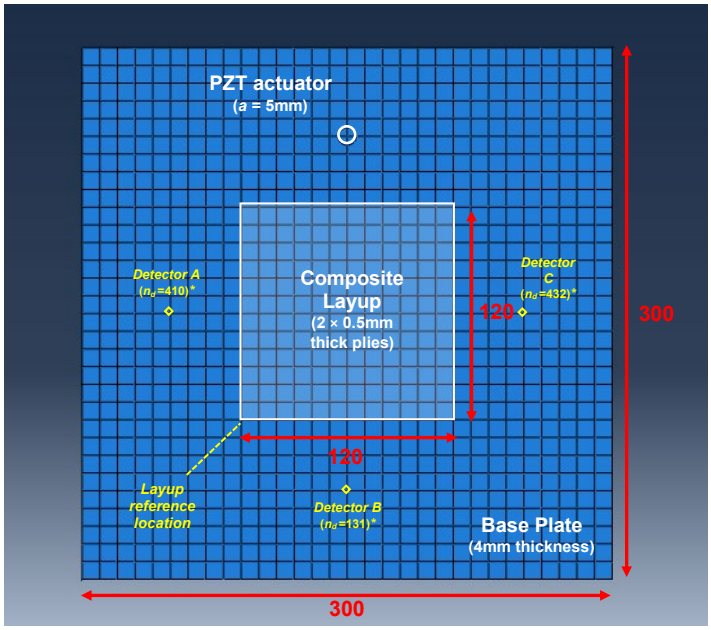

	Dimensions (mm)	Material
Base Plate	300×300×4	Aluminium
Layup (each ply)	120×120×0.5	Simulated CFRP composite material (Type I or Type II)

Table 7: Numerical Simulations: Case Summary

Case Description	No. Layup Plies	Layup Material	Changes Imposed on Layup	No. Cases	Output
Base Case (No Layup)	0	-	-	1	$\boldsymbol{U}_{\{0\}}$
Layup Only Cases	1	m $m \in \{I, II\}$	-	2	$\boldsymbol{U}_{\{m\}}$
'Single Change' Cases	1	m $m \in \{I, II\}$	a $a \in \begin{Bmatrix} D1, D2, D3 \\ P1, P2, P3 \end{Bmatrix}$	12 (2 × 6)	$\boldsymbol{U}_{\{m,a\}}$
Dual Change Cases	1	m $m \in \{I, II\}$	a and b $a,b \in \begin{Bmatrix} D1, D2, D3 \\ P1, P2, P3 \end{Bmatrix}^*$	30 (2 × 15)	$\boldsymbol{U}_{\{m,a,b\}}$

Note: $a \neq b$ for these simulation cases.

The differing dimensions for the base and the layup sheets arise due to a set of modelling constraints. First of all, the total number of elements within the finite element model requires to be kept to a *reasonable limit*, to ensure an acceptable simulation time. Secondly, the mesh size and the simulation timestep must be sufficiently small to ensure that the guided waves propagating in the base plate and the layup materials can be simulated with *good accuracy*. Shen & Giurgiutiu (2015) recommend a maximum element size Δx^{max} of the order of one-twentieth the smallest mode wavelength λ_{min}, and a maximum timestep Δt^{max} of the order of one-twentieth of the shortest wave mode travel time t_{min} ($=\lambda_{min}/c_{max}$). Finally, it is necessary

to have a *consistent mesh* in all simulations, i.e. a mesh whose nodes are fixed, and are not adjusted, in order to maintain *consistency* in simulation output.

Table 8 indicates the maximum mesh size and maximum timestep constraints, for the base plate and the composite layup materials, based on the recommended limits given above. (These calculations are based upon a carrier frequency $f_c = 280$kHz, and nominated frequency-thickness products $f_c\, d$ = 1.12 MHz.mm for the base plate and $f_c\, d$ = 0.28 MHz.mm for the layup material; however it should be noted that the results are only weakly sensitive to the nominated material thicknesses)[6]. The maximum mesh size is the order of 0.4mm within the base plate, and of the order of 0.2mm in the layup, while the overall maximum timestep taking into account both materials is of the order of 20 ns. These limits are governed by the wavelengths of the antisymmetric A0 modes travelling in the materials, and also the longitudinal wave velocity for disturbances travelling along the carbon fibres.

When the mesh sizes shown in Table 8 are considered together with a limit on the *maximum number of model elements, n*, it becomes apparent why a scaled-down model must be constructed. If a nominated limit of $n = 8 \times 10^6$ is imposed[7], model volumes must be reduced by a factor $v = 0.23$ to maintain mesh densities (that is to say, model lengths should be reduced by a factor $l = v^{1/3} \sim 0.6$). This constraint must however be balanced against the requirements that mesh should be *uniform* and *regular* [8] [9] ,that nodes should *coincide* at the base plate and the layup surfaces (i.e. $\Delta x_b = \Delta y_b = \Delta x_l = \Delta x_l$), and that *each layup ply should be discretized* to some level, for good accuracy. It is not possible to satisfy all these constraints simultaneously, and therefore a compromise is reached which is summarized in Table 5. The x and y dimensions of the base and the layup materials are reduced by factors of $^2/_5$, but the thickness of layup plies is doubled, to ensure layup discretization. This reductions result in a "base case" model with 9 million nodes. However, this model does not satisfy mesh density requirements, so a "high density" model comprising 19 million nodes is also developed. The base case model is used in the majority of simulation studies, however, selected cases are re-run with the high density model, to confirm that there is no significant impact on the simulation accuracy.

[6] The calculations additionally assume that carbon-fibre layup material is *fully cured*, and also that the wave modes propagate *independently* within the base plate and the layup material.
[7] In this context, this is a 1-day simulation run time, based on a 4-node allocation on a Sheffield university Sharc cluster facility.
[8] i.e. constructed from cuboid elements.
[9] Note that additional meshing constraints apply in the vicinity of the PZT actuator. These constraints are described in the section which follows.

Table 8: Model Development: Maximum Mesh Size and Minimum Timestep Constraints

Model Component	Limiting Criteria		Resultant Constraints	
	Mode Wavelengths [1] λ_{min}	Material Bulk Wave Velocities c_{max} [3]	Maximum Mesh Size Δx^{max}	Maximum Timestep Δt^{max}
Aluminium Base Plate	18.9 mm (S_0 mode) 8.6 mm (A_0 mode)	6200 m/s	0.43 mm (13 elements /mm^3)	69 ns
Carbon Fibre Composite Layup	21.4 mm (S_0 mode) [2] 4.3 mm (A_0 mode) [2]	11480 m/s	0.21 mm (108 elements /mm^3)	18 ns

Note 1: The wavelengths are based on based upon a carrier frequency f_c = 280kHz, and nominated frequency-thickness products $f_c\,d$ = 1.12 MHz.mm for the base plate, and $f_c\,d$ = 0.28 MHz.mm for the layup material. However, it should be noted that the minimum wavelengths are only weakly sensitive to nominated material thicknesses.
Note 2: These wavelengths are based upon on approximate mode velocities c_{S0}~6000 m/s; c_{A0}~1200 m/s in fully-cured CFRP material, at nominated frequency-thickness product $f_c\,d$ = 0.28 MHz.mm, reported by Pierce *et al* (1996). Again, the wavelengths are only weakly sensitivity to nominated material thickness.
Note 3: The maximum longitudinal wave velocities are calculated from the expression $c_L = \sqrt{E(1-\upsilon)/(\rho(1+\upsilon)(1-2\upsilon)}$, where E is material Young's modulus and υ is material Poisson ratio. The Young's modulus for the composite material in the direction of the carbon fibres, which is 166 MPa, is applied in this calculation for conservatism.

Table 9: Finite Element Model: Dimensions, mesh discretization, mesh density and total numbers of elements

		Base Plate	Composite Layup (each ply)	Total
Model Data	Dimensions (mm)	300 × 300 × 4	120 × 120 × 0.5	-
	Volume	360 cm^3	72 cm^3	432 cm^3
Scaling Factors[1]	Length	$^3/_5 \times {}^3/_5 \times {}^2/_5$	$^3/_5 \times {}^3/_5 \times 2$	-
	Volume	0.14	0.72 [2]	0.15
Base Case FE Model	Discretisation (Δx/ Δy/ Δz)	0.33/0.33/0.40	0.33/0.33/0.25	-
	Element density	22/mm^3	36/mm^3	-
	No. Elements	8.1 × 10^6	0.5 × 10^6	8.6 × 10^6
High Density FE Model	Discretisation (Δx/ Δy/ Δz)	0.25/0.25/0.33	0.250.25/0.125	-
	Element density	48/mm^3	128/mm^3	-
	No. Elements	17.2 × 10^6	1.8 × 10^6	19.0 × 10^6

Note 1: Scaling factors relate the simulation model dimension to physical benchtest model dimensions, shown below Figure 7.
Note 2: Figures based on two plies, each of thickness 0.5mm.
Note 3: Simulation timestep is 20ns for "base case model", and 10ns for "high density model".

6.2 Material Properties

Table 10 and Table 11 summarize the physical properties of the base plate and the composite layup materials assumed in simulation studies. The properties of the aluminium base plate material are firmly defined. However, the properties of the pre-preg layup material are subject to considerable uncertainty, due to a notable lack of experimental data. The pre-preg consists of a high-strength carbon fibres embedded in a *part-cured* epoxy matrix; as such, the composite material has anisotropic and viscoelastic properties. While the long-term response of such material to impulse loads has been measured experimentally (Lukaszewicz & Potter, 2012), the short-term response of such material to loads applied at ultrasonic materials remains completely unknown.

To get around this issue, two types of layup material are considered in simulation studies, denoted as *upper limit* (Type I) and *lower limit* (Type II) materials. The upper limit material is a *fully-cured* carbon fibre composite material, having properties which are taken from data provided by Kim *et al* (2015). This material is anisotropic, but also perfectly elastic. The lower limit material is a part-cured *pure epoxy* material which has frequency-dependent properties based on data provided by O'Brien, Mather and White (2001) that are illustrated in Figure 20. This material is visco-elastic, but is also isotropic.

A real pre-preg composite material is thus expected to have physical properties which lie *somewhere between* the upper and lower extremes defined by Table 1, but at a point which is not known. In the analysis that follows, the type of layup material which is considered in any given simulation study is indicated within bracketed subscripts which succeed the variables $\boldsymbol{U}$, $\boldsymbol{Y}$ and $\boldsymbol{t}$ (for example $\boldsymbol{U}_{\{M1\}}$ or $\boldsymbol{U}_{\{M2\}}$). The Type I material is considered as 'base case', and the Type II material is considered as a 'sensitivity case'.

Table 10: Material Properties (1): Aluminium Base Plate (20°C)

Density	Young's Modulus			Poisson Ratio			Shear Modulus		
	E_1	E_2	E_3	ν_{12}	ν_{13}	ν_{23}	G_{12}	G_{13}	G_{23}
kg/m³	GPa	GPa	GPa	-	-	-	GPa	GPa	GPa
2700	70.0			0.33			26.3		

Table 11: Material Properties (2) – Pre-Preg Carbon Fibre Composite

		Density	Young's Moduli			Poisson Ratios			Shear Moduli		
			E_1	E_2	E_3	ν_{12}	ν_{13}	ν_{23}	G_{12}	G_{13}	G_{23}
		kg/m³	GPa	GPa	GPa	-	-	-	GPa	GPa	GPa
Upper Limit: Fully Cured CFRP Material		1570	166.0	8.56	8.56	0.269			0.269	0.456	5.60
Lower Limit: Uncured Epoxy	*∞ Hz*	1173	0.172	0.172	0.172	0.35			0.464	0.464	0.464
	280 kHz		5.7×10^{-4}	5.7×10^{-4}	5.7×10^{-4}				1.5×10^{-3}	1.5×10^{-3}	1.5×10^{-3}
	0 Hz		4×10^{-11}	4×10^{-11}	4×10^{-11}				1.2×10^{-10}	1.2×10^{-10}	1.2×10^{-10}

Figure 22: Pure EPON862 Epoxy Shear Modulus, as function of frequency (O'Brien *et al*). Data for cure parameter α = 0 (black line) are assumed as a limit case.

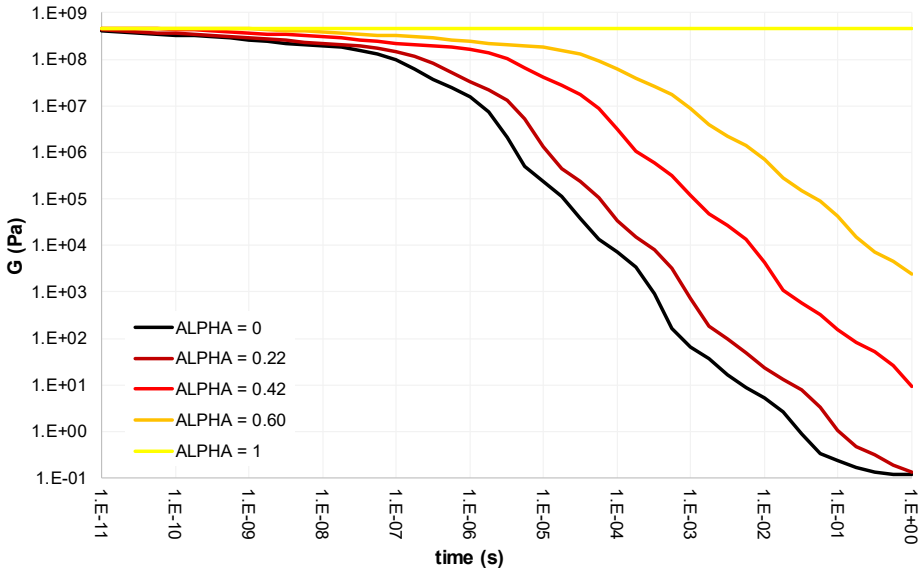

6.3 Modelling of PZT Actuator

The 4 mm thick aluminum base plate requires to be excited by the modulated waveform (shown in Figure A), through a d = 10mm diameter PZT transducer. This actuation will predominately generate S0 and A0 modes in the base plate (as shown in Figure 5a).

Direct simulation of the piezolectic material within the PZT actuator involves the conversion of electrical signals into mechanical vibrations, and is prohibitvely expensive from a computational viewpoint. In order to get around this problem this study assumes that the actuator is *perfectly bonded* to the base plate (i.e. that the actuator is attached to the base plate by an infinitely thin and infintely strong bonding layer). Under this assumption, the voltage which is input to a circular PZT transducer is delivered to a base plate as a concentrated line load which acting normally to the actuator perimeter (Giurgiutiu, 2003). Therefore, the actuator can be *elminated* from the simulation model.

Line loads require to be applied as point loads at mesh nodes in finite element models. Therefore, the mesh in the actuator region must be carefully specified. Figure 23 illustrates this mesh (for the 'standard density' model); the nodes are evenly spaced and symmetric around the x- and y- axes, allowing point loads to be applied at equal angular intervals. (A similar mesh, with identical point loads, is created for the 'higher density' model). This loading arrangement produced near-ideal circular-crested Lamb waves, which (as shown below) are in very good agreement with analytic predictions.

Figure 23: Actuator Region Mesh and Radial Point Loads (Standard Density Mesh Model)

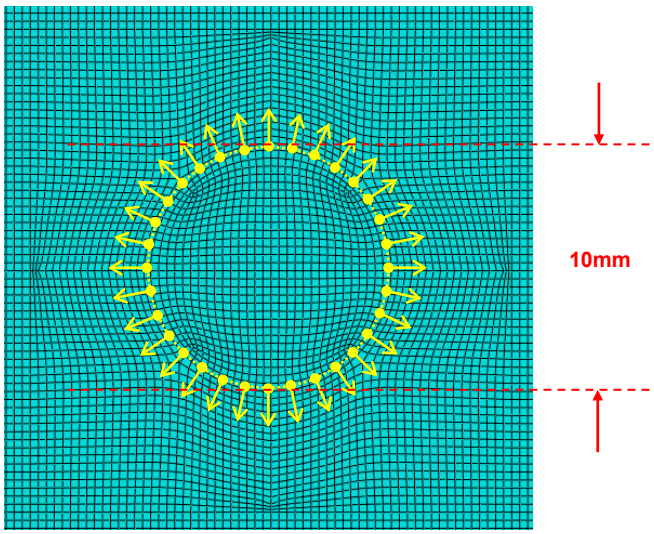

6.4 Modelling of PZT Detectors

As with the actuator, the simulation of the piezoelectric processes which occur within the detector units is computationally expensive. In order to accelerate simulations to point of being viable, it is assumed that the piezoelectric material lying under each detector unit surface is *infinitely thin*, and that this material *does not interact electro-mechanically* with the base

plate[10]. This assumption becomes increasing valid, as the size of each detector unit becomes increasingly small. Under these assumptions, the displacement field $\boldsymbol{u}(x, y, t)$ which occurs upon on the surface of the base plate may be assumed to be unaffected by each detector units, and it follows that the detector units may then be *eliminated* from the simulation model.

As discussed in subsection 1 above, the base plate has been meshed using cubic elements whose nodes are spaced at *regular intervals* ($\Delta x_b = \Delta y_b = 0.33$mm). The detector unit nodes ideally need to coincide with these mesh nodes, to maintain simplicity and to ensure simulation accuracy. The simplest way to meet this requirement is to model the detectors as *square-shaped* units whose edges are located at four mesh nodes, A, B, C, D, and whose centre is located at another mesh node O, as shown as Figure 24. To satisfy the requirement that the unit be as *small as possible*, this unit must have occupy five nodes with side length of $\sqrt{2}\Delta x$, and thus have a footprint area of $2\Delta x^2 = 0.22\text{mm}^2$.

The surface displacement fields which are recorded at the detector nodes, $\boldsymbol{u}(x, y, t)$, remain to be converted into a virtual output voltage signal, $V(t)$. This conversion is performed by assuming that the output voltage is proportional to the sums of normal strains across the detector surface, as has been proposed by Yeum, Sohn and Ihm (2011). For the minimally sized and square-shaped virtual detector unit shown in Figure 24a, these normal strains are simply given as:

$$\varepsilon_i = \left\{\frac{u_{iA}+u_{iD}}{2} - \frac{u_{iB}+u_{iC}}{2}\right\}/\sqrt{2}\,\Delta x \qquad \varepsilon_j = \left\{\frac{u_{jA}+u_{jB}}{2} - \frac{u_{iB}+u_{iC}}{2}\right\}/\sqrt{2}\,\Delta x$$

where the orthogonal vectors i and j and the displacement components u_i and u_j at nodes, A, B, C and D are parallel to the detector unit edges. From the calculated ε_i and ε_j strains, a virtual output voltage V is given by:

$$V = c\bar{\varepsilon} = \frac{1}{2}\, c\,(\varepsilon_i + \varepsilon_j)$$

where c is an arbitrary proportionality constant which reflects the electro-mechanical properties of the piezoelectric material.

While this modelling approach avoids excessive computational effort, a drawback is that each virtual detector unit has a small footprint (0.22mm^2, vs. 79mm^2 for each of the physical PZT detectors which are shown in Figure 6). Such a small detector unit is probably unviable in practice, as its output signals would be likely be dominated by noise. As a partial workaround, a second model has been constructed where the base plate is covered in *larger* virtual detector units, having the side length of $3\sqrt{2}\Delta x$ and footprint area of $18\Delta x^2 = 2\text{ mm}^2$, as shown in Figure 24b [11]. The results from this model will be studied as a sensitivity case. However, it is still assumed that there is *no interaction between each detector unit and the base plate*.

[10] Under these conditions, the two electrodes of each piezoelectric transducer detector unit would be able to sustain an electrical potential difference, without having to apply strains which would bend and deform the base plate surface.

[11] For this model, the calculation of the virtual voltage requires summations of displacements at the twelve boundary nodes shown.

Figure 24: 'Virtual PZT detector units' as constructed from the base plate surface mesh nodes

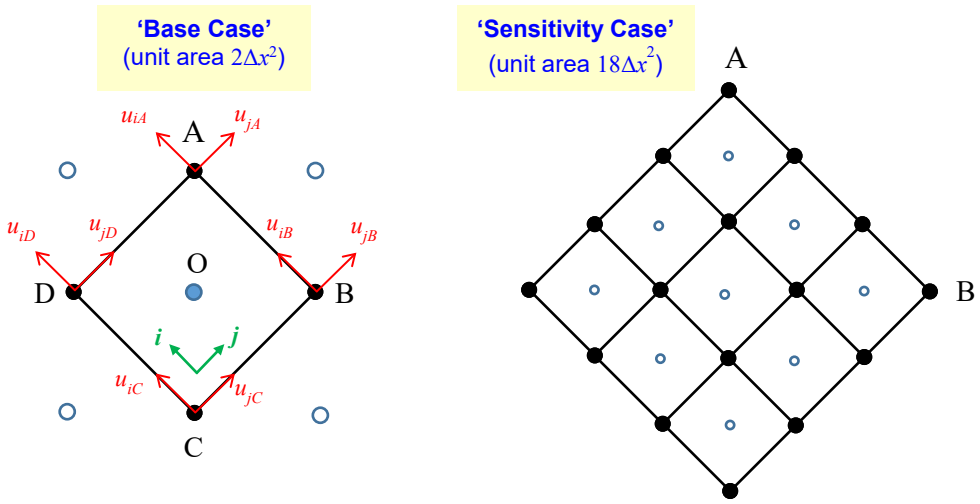

6.5 Modelling of Changes in Environmental Conditions, and Modelling of Defects

Simulation output may be affected by *environmental changes*, as well by *defects* which are introduced into the layup material. It is therefore necessary to simulate both these classes of upsets, such that it can be confirmed whether or not the former class can be distinguished from the latter.

The complete set of possible defects and environmental changes which could affect the manufacture process is a very highly-dimensioned space. There are almost unlimited possible *shapes*, *sizes*, *locations*, and *orientations* for defects; each of these defects could occur *independently*; in *different layers* of the layup material. Furthermore, the ambient temperature, and the reference point (i.e. position at which the material is laid down on the layup surface) could also vary independently. To keep the number of simulation cases to a reasonable level, three simplified sets of defect and three simplified types of environmental change are considered in this study, which are described in Table 12.

The three defects, labelled D1, D2 and D3, may be described as "cluster of dispersed objects", a "strip defect", and a "large discrete defect". These defects are located at the positions shown in Figure 25. These objects are intended to simulate, crudely, entrainment of *small debris* during the layup process, a *tow gap* in the layup sheet, and a *large foreign object* or a *trapped air bubble*. All three objects have simplified shapes, extend through one half of the total layup sheet thickness (i.e. 0.5mm), and are coincident with the mesh nodes on the base plate surface such that the simulation accuracy is maintained.

The three environmental upsets, labelled P1, P2 and P3, are intended to assess the effect of a small shift in the *layup reference point* (simulated by moving the layup by 1mm in the x- and y- directions), a small shift in the *placement robot orientation* (simulated by re-orienting the carbon fibres by 2 degrees) and a small variation in *ambient temperature* (1°C, simulated by adjusting the physical properties of the aluminium base plate material).

Critically, all six of the imposed changes which are defined in Table 12 can occur *independently* of one another. If the total number of upsets is denoted by n, this is to say that the total number of possible simulation studies which could be simulated based on the six upsets, j, is given by the factorial sum $j = \Sigma_{m=1}^{m=n} n!/(m!\,(n\text{-}m)!)$, in which the variable m indicates how many upsets are occurring simultaneously. This sum total is 63, i.e. there are a relatively large number of *potential* simulation cases. It is, however, not beneficial to perform all these 63 simulations, for reasons of simplicity and clarity. In this study a maximum of two upsets will be simulated simultaneously, such that variable $m \in \{0, 1, 2\}$. As a result the total number of simulation cases j becomes 1 + 6 + 15 = 22.

In the analysis sections which follows, specific changes are distinguished by appending subscripts to the arrays $\boldsymbol{U}$, $\boldsymbol{Y}$ and $\boldsymbol{t}$. To give an example, the expression $\boldsymbol{U}_{\{D1,P1\}}$ refers to the data which are output from virtual detector units, when the type D1 defect and the environmental change P1 are modelled simultaneously.

Table 12: Enviromental changes and defects, considered for simulation studies.

Environmental Changes		Defects	
Label	**Description**	**Label**	**Description**
P1	Ply Offset (Δx=Δy=1 mm shift relative to reference point shown)	D1	Group of 20 small dispersed defects.
P2	Ply Rotation (2° rotation of carbon fibures, clockwise from y-axis)	D2	Single strip defect.
P3	Change in Aluminum properties, due to a 1°C temperature increase[1].	D3	Single large square defect.

Note 1: Applied gradients: Young's modulus: -450 ppm C^{-1}; Density -67.5 ppm C^{-1} and Poisson Ratio 56 ppm C^{-1}

Figure 25: Locations of Defect Groups D1, D2 amd D3.

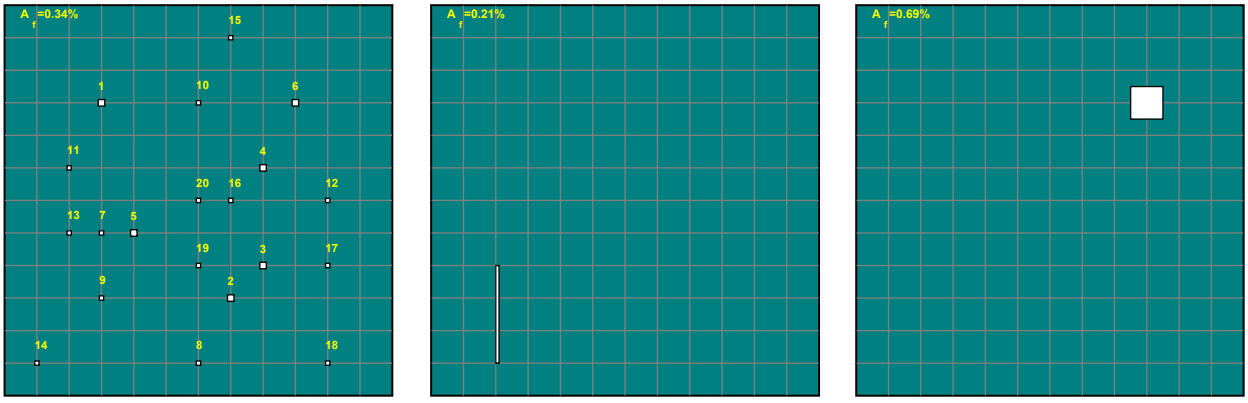

Defects located in the lower 0.5mm layup layer

Defect located in the upper 0.5mm layup layer

Defect located in the upper 0.5mm layup layer

VII. Simulation Results Analysis

In this section, the output data from the numerical simulations are discussed. This discussion is split into five subsections, of which the first two subsections focus upon *time-series output*. Section 7.1 is an assessment of *simulation accuracy*, and Section 7.2 is a discussion of *virtual output data*, which also includes an examination of the amounts of energy contained within the composite layup materials.

The following three subsection focus upon the *features* which are derived from the simulation output using the threshold level algorithm. Section 7.3 discusses *general properties* of these features and general properties of change features. This analysis including sensitivity studies which address impact of mesh refinement, detector unit size, and layup material type. Section 7.4 then discusses *classification* of defects, based upon the three types of synthetic defects which have been simulated as shown in Figure 25. Finally, Section 7.5 presents *summary statistics* which may be used to compare features against those obtained from the physical benchtests.

7.1 Comparison against Analytic Solution

The accuracy of the simulation model is first assessed, by comparing output surface displacement components against an analytic solution which exists for circular-crested Lamb waves (Giurgiutiu, 2003) which is shown in Appendix A.

Figure 26 compares radial components of displacement $r_r(t)$ for two points on the surface of the base plate at distances r = 0.05 m and r = 0.2 m from the actuator against analytic predictions (x-co-ordinate x_d = 0 m, and detector indices n_d = 566 and n_d = 131). The simulation output and the analytic solution are initially very closely matched. This is particularly evident if envelope features $y_r(t)$ are extracted from $r_r(t)$ and plotted on a logarithmic scale, as shown in the second row of Figure 24 [12]. The difference features $\Delta y_r(t)$, shown by the green lines, are initially very small.

After approximately 50μs, the simulation output and the analytic solution start to diverge. This divergence occurs because the analytic solution applies to an infinite, *unbounded* plate, whereas the simulation model is for a finite, bounded plate. The difference between the analytic solution and the simulation model may thus be attributed to the reflections which occur at plate boundaries.

In general, when guided wave pulses reflect from plate boundaries, they generate *shear horizontal wave modes* (Shen & Giurgiutiu, 2015). Figure 27 compares the simulation output shown in Figure 26 to hypothetical solutions which would be obtained if the guided wave pulses reflected from the plate boundaries *without* generating these shear horizontal wave modes. The simulation output and the hypothetical solutions diverge very quickly, from which it may be concluded that significant quantities of these modes are generated upon each boundary reflection, and that these modes quickly dominate the system response. It is implied that the field which is produced by the actuator pulse will rapidly become *incoherent*, and will cease to carry useful information.

[12] This process is described in Section 3.3 above.

Figure 26: Radial components of displacement components, r_r , at two locations on surface of base plate. (No Layup).

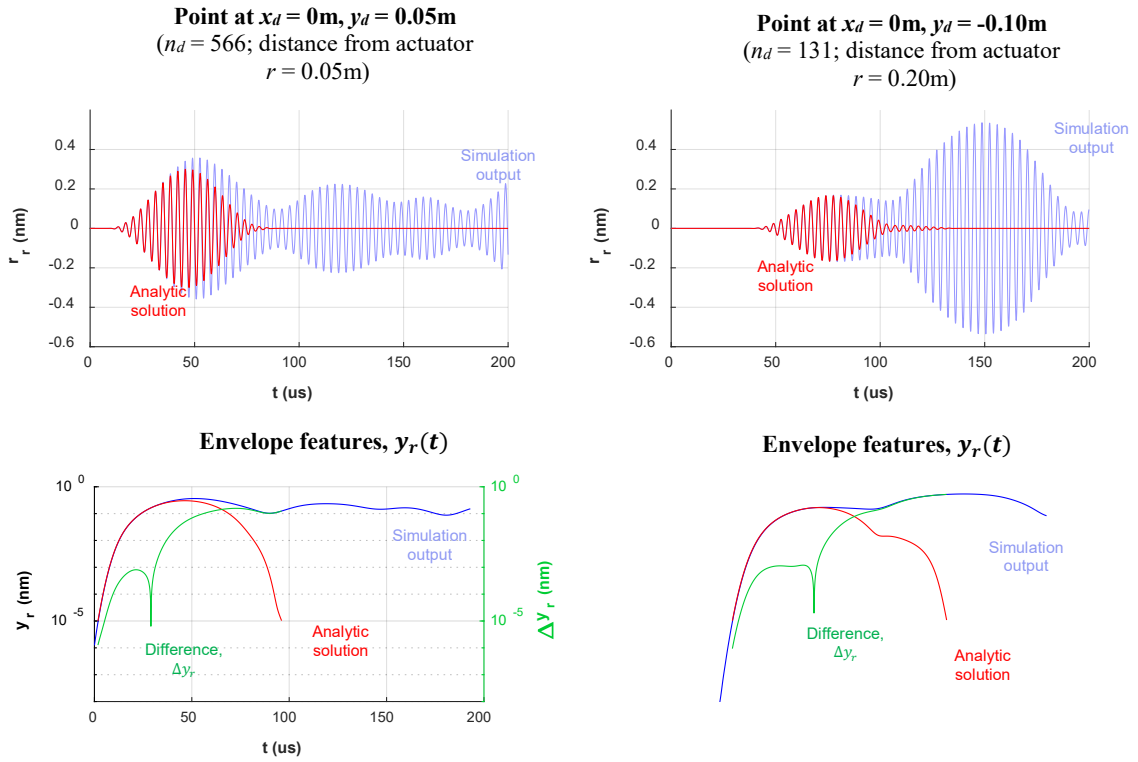

Figure 27. Revised analytic solution, based on Lamb wave components reflected at plate boundaries, but *not* including shear horizontal wave mode conversions occurring at plate boundaries.

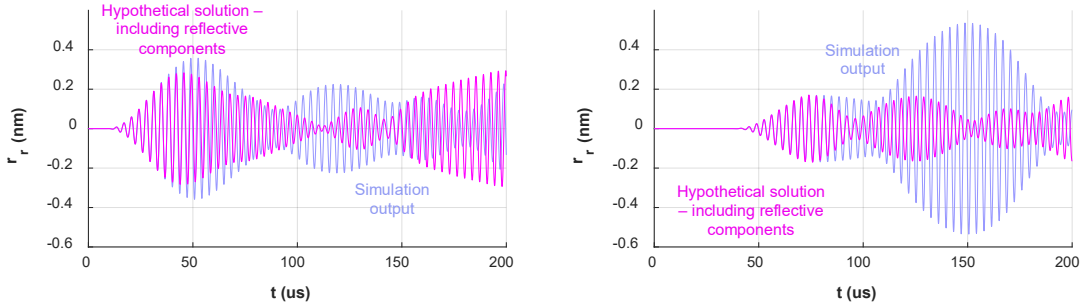

7.2 Time-Series Data Analysis

In this section, properties of the time-series data produced by the simulations, $\boldsymbol{U}(t)$, e(t), and $\boldsymbol{Y}(t)$, are described. The data $\boldsymbol{U}(t)$ are initially *normalized*, based on the maximum amplitude of the $\boldsymbol{u}(t)$ data obtained from the detector located beneath the actuator unit during the actuation process. That is to say, the data are normalized such maximum amplitude of the data obtained from the detector n_d = 711, within the time limit t < 71.4 μs, is unity.

Figure 28 compares the $\boldsymbol{u^n}(t)$ data obtained from the virtual detector unit having index n_d = 121, against the corresponding radial component of surface displacement $\boldsymbol{r}(t)$. This image that

that $\boldsymbol{u}(t)$ is different from $\boldsymbol{r}(t)$, since it is based upon the sums of strains which do not necessarily occur in radial directions. The $\boldsymbol{u}(t)$ feature bears qualitative similarity to the feature obtained from the benchtests which is shown in Figure 8.

Figure 28: Radial displacement component $r_r(t)$ and virtual output data $u_{\{0\}}$, for virtual detector unit n_d = 131 (No Layup)

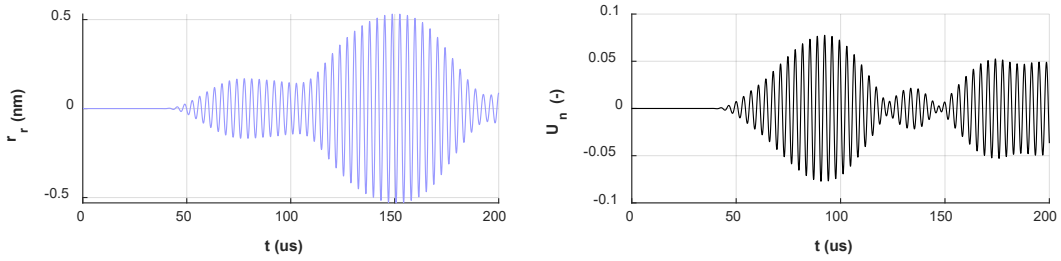

Figure 29 shows *groups* of $\boldsymbol{u}_{\{0\}}^{\boldsymbol{n}}(t)$ vectors which are obtained from a *single row* of virtual detector units, and a *single column* of virtual detector units. The central portions of these images are magnified for interest, and shown below (note, these magnified images were produced by performing an additional simulation where detector units were space at intervals Δx_d = 0.33mm). These images shown that, under ideal, that output data will vary smoothly as the mounting location of the detector is changed.

Figure 29: Virtual output data from a single row and a single column of detector units (No Layup).

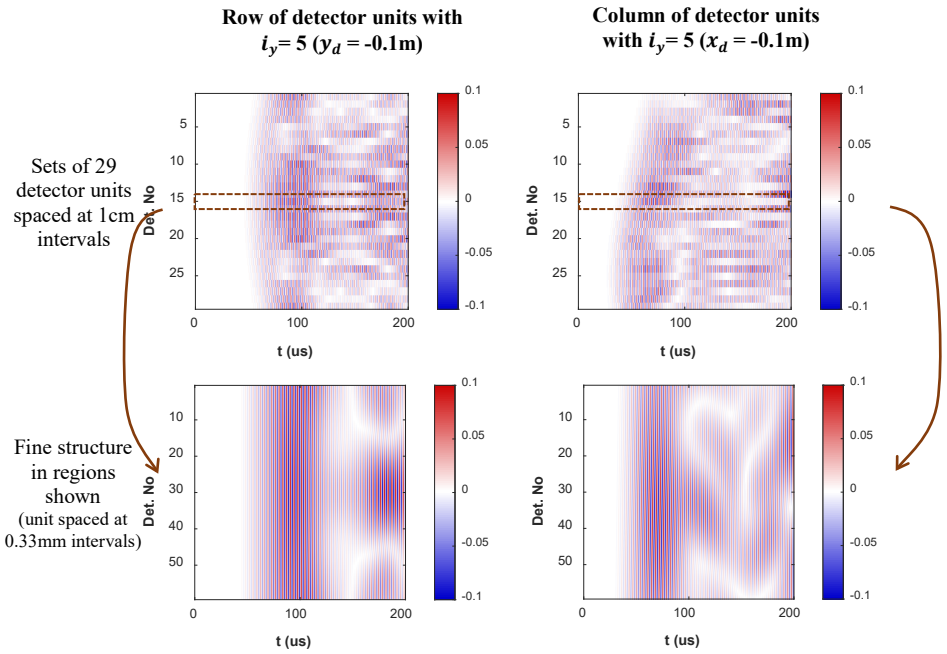

Figure 30 compares the effect that the *layup material* has upon the groups of $\boldsymbol{u}^{\boldsymbol{n}}_{\{0\}}(t)$ output vectors which were featured in Figures 28 and 29. The Type I layup material (hard-cured carbon fibre composite) has a more significant effect on the output than the Type II layup material (uncured epoxy). The output which would be expected if a real pre-preg sheet had been simulated (i.e. a *part-cured* carbon fibre composite material) would be expected to lie somewhere between these two extremes.

Figure 31 illustrates the proportions of the total input work energy within the base plate and the layup layers, $e(t)$, for the two layup materials. The Type I material draws around 1% of the input work energy from the base soon after actuation commences. and this energy is retained. By contrast, the Type II material draws less than 0.1% of the input work energy from the base, which is concentrated in the lower 0.5mm layup layer, and this material also dissipates the energy of the base plate, as it is visco-elastic. Once again, the output which would be expected if a real pre-preg sheet had been simulated would be expected to lie somewhere between the extremes.

Before the data can be used to extract time-of-arrival features, they must be *convoluted* to extract the signal envelopes. Figure 32a shows the entire *convoluted feature* $\boldsymbol{Y}_{\{0\}}$ which is obtained with no layup, with the $\boldsymbol{y}_{\{0\}}$ data produced by the detector unit located at the actuator transducer being indicated by the red line. The data indicate that the actuation pulse *reduces in its intensity* with distance travelled. This observation is further confirmed by Figure 32b, in which the peak amplitudes of convoluted features, y^{max}, are plotted as a function of the normalized actuator-detector separation distances, r / a [13]. These data are clustered around the line $y_{max} = a/\sqrt{r}$, indicating that roughly speaking, the wave intensity reduces as a function of distance *squared*.

Finally in this section, it is informative plot the threshold level features $\boldsymbol{t}$, which are obtained when the $\boldsymbol{Y}_{\{0\}}$ features are input to the threshold level algorithm, as a function of the normalized separation distance r / a [14] (Figure 32c). These features lie very close to the line defined by equation $t = r/c_{g(S0)}$, where $c_{g(S0)}$ is the S_0 mode group velocity. This result confirms that the when the waveform shown in Figure 5 is applied to the nodes shown in Figure 23 as a set of radial loads, an S_0 wave is produced.

[13] The y^{max} values are evaluated using feature data up to a cut-off time limit $t = r/c_{g(S0)} + t_d$ only (where $c_{g(S0)}$ is the group velocity for the S0 wave mode and t_d is the duration of the actuation pulse shown in Figure 2).

[14] Features time-of-arrival calculations are based upon a nominated threshold level θ= 0.001

Figure 30: Impact of Layup Material upon U_n Samples

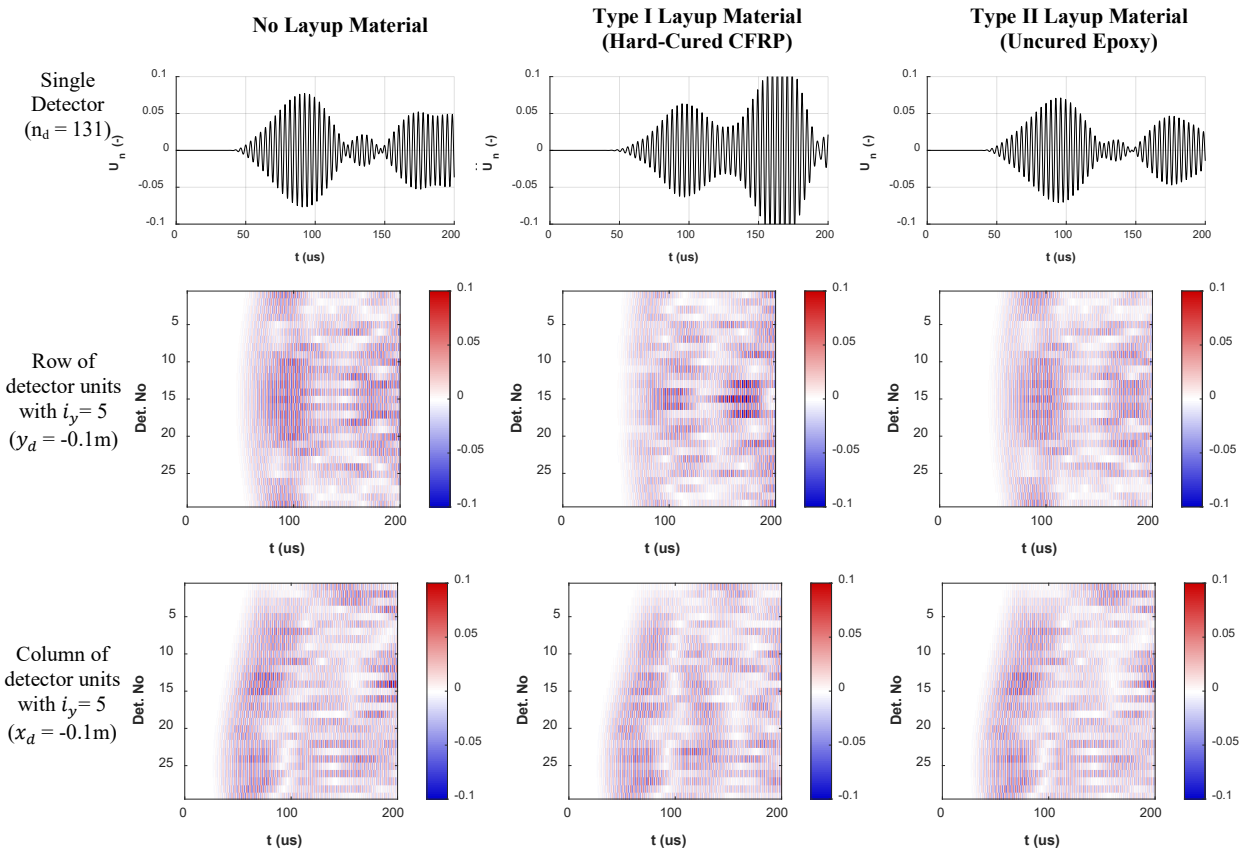

Figure 31: Proportions of actuator input work energy present within the base plate and the two 0.5mm composite layup layers, *e*(*t*)

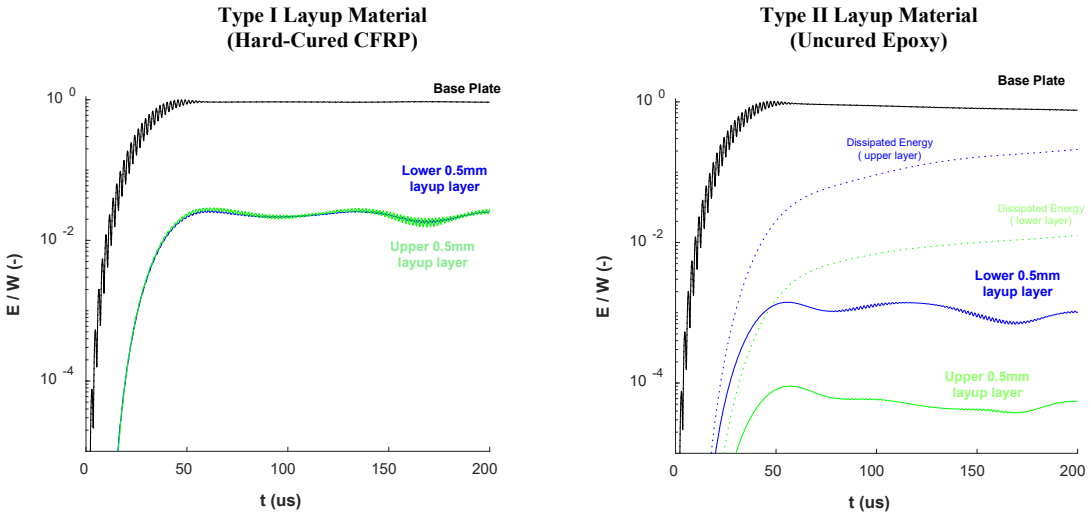

Figure 32: Convoluted output data, $Y_{\{0\}}$, and corresponding peak amplitude features y^{max}, and threshold level crossing time features, $t_{\{0\}}$, as a function of the normalized actuator-detector distance r/a.

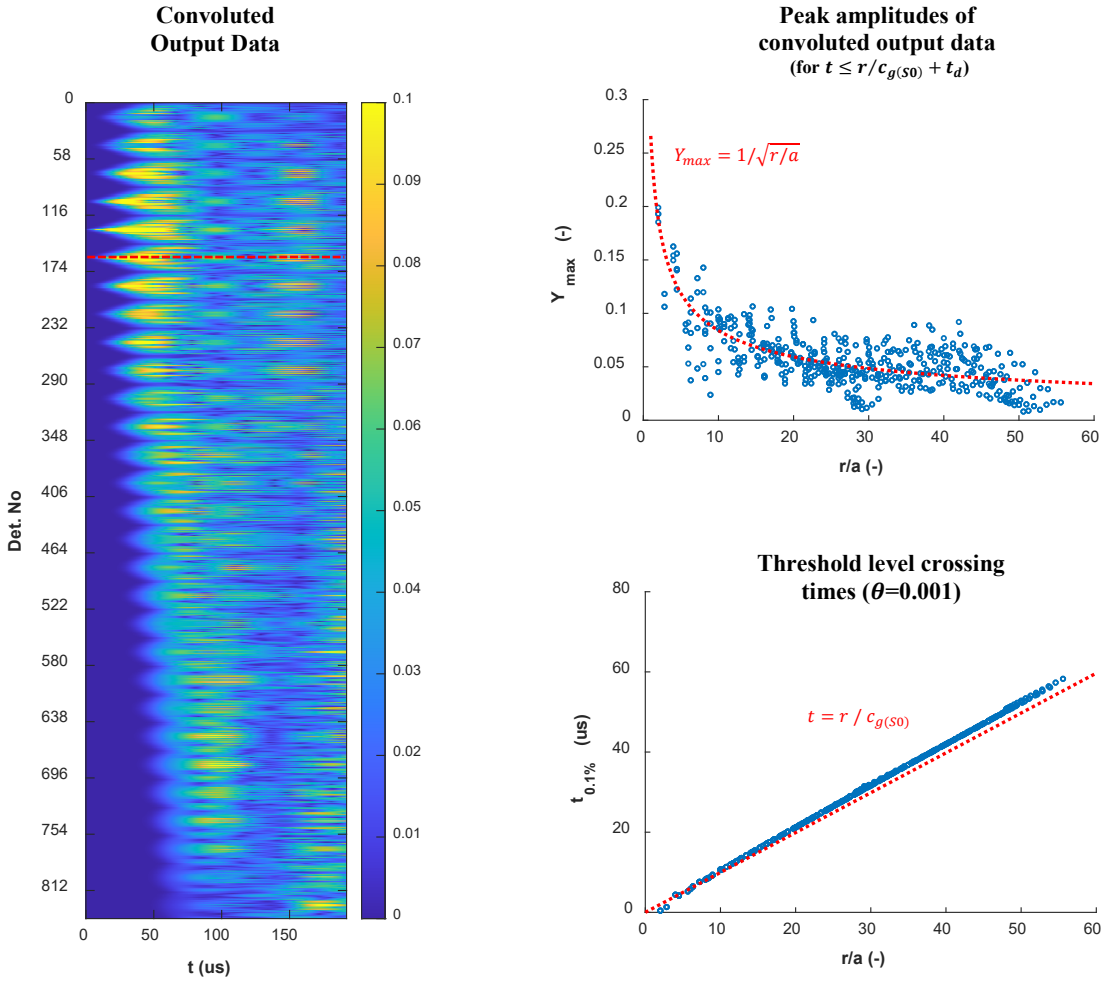

7.3 Feature Analysis

The convoluted data $\boldsymbol{Y_n}$ is converted into a feature vector $\boldsymbol{t}$ using a threshold level algorithm, and therefore (as for the experimental benchtests) a suitable value for threshold level parameter θ must be selected to produce satisfactory results.

Figure 33 shows, as a series of pixelated images, the feature $\boldsymbol{t}_{\{0\}}$ obtained using the threshold level parameters $\theta = 0.001$, $\theta = 0.01$, and $\theta = 0.1$. When the parameter θ is set at the lowest level, the component entries of $\boldsymbol{t}$ are (to a very close approximation) proportional to the transducer separation distance r as was illustrated in Figure 30c. However, as the parameter θ is increased, wave reflections from the lower edge of the base plate begin to upset this relationship. Furthermore, when $\theta = 0.1$, the threshold algorithm misses the rising edge of the S_0 wave mode entirely; this causes a large increase in $\boldsymbol{t}$ values (note the modified time scale). For this reason, $\theta = 0.01$ is a *preferred threshold level parameter* and it is applied to produce the images which appear in the following subsections.

Figure 34 shows the *change* feature vectors $\Delta\boldsymbol{t}_{\{1\}\{0\}}$ which are obtained when a 1mm layer of Type I (CFRP) material is attached to the base plate ($\theta = 0.001$, $\theta = 0.01$, and $\theta = 0.1$). These

$\Delta \boldsymbol{t}$ vectors are again displayed as pixelated images, with the boundaries of the layup region illustrated by the dotted lines. As per the physical benchtests, the component entries of $\Delta \boldsymbol{t}$ have *positive* values. These positive values indicate that the layup material has *delayed* the arrival of the S_0 wave mode at detectors. Moreover, the images reveal that these positive values increase in size as the amount of layup lying above the path between the actuator and a detector increases. This fact infers that the layup material is *absorbing the actuation pulse* energy, as is also shown by Figure 31a. If a line of detectors is followed outwards from the actuation point, the Δt values increase *until the edge of the layup is reached*. As a result, the images contain 'shadows', in regions which lie 'behind' the layup.

Figure 33: $\boldsymbol{t}_{\{0\}}$ feature images. (Base plate only - no layup material)

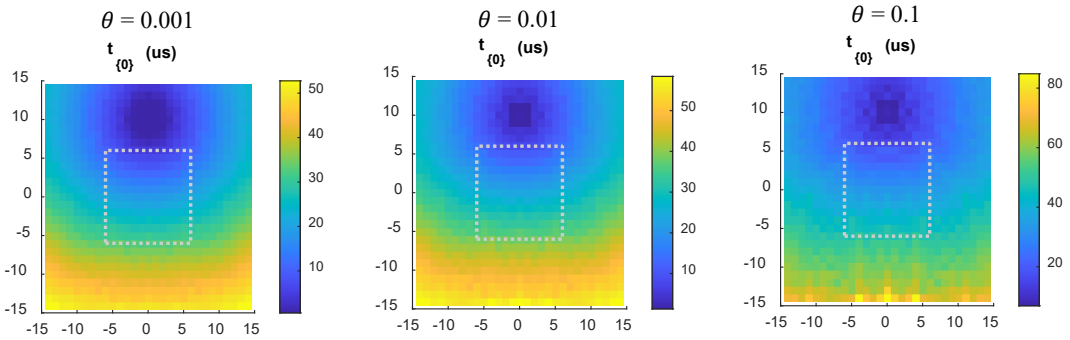

Figure 34: $\Delta \boldsymbol{t}_{\{1\}\{0\}}$ change feature images (Base plate with Type I layup material)

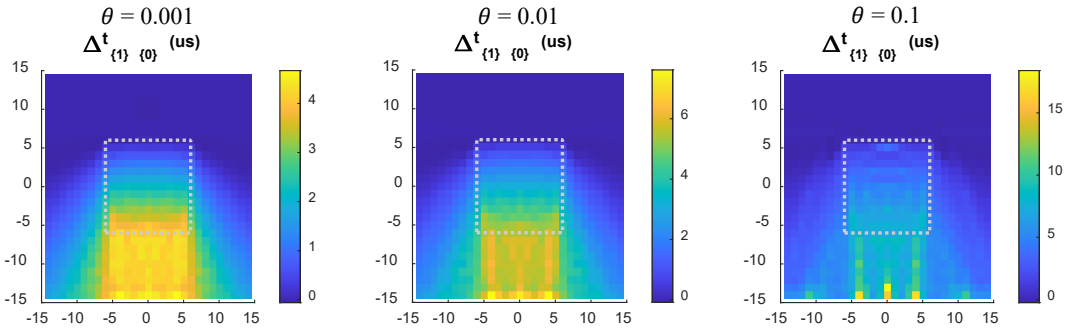

Figure 35 shows change features which are obtained when a *defect* of type D3 and an *environmental change* of type P1 are imposed upon the layup (Type I material, with θ = 0.01) [15]. The images in the left-hand columns show changes relative to the features obtained with *no layup*, i.e. $\Delta \boldsymbol{t}_{\{1,D3\}\{0\}}$ and $\Delta \boldsymbol{t}_{\{1,P1\}\{0\}}$. These images are virtually indistinguishable from the central image in Figure 34 above. The figures in the right-hand columns show the changes relative to the features obtained *with* the layup, i.e. $\Delta \boldsymbol{t}_{\{1,D3\}\{1\}}$ and $\Delta \boldsymbol{t}_{\{1,P1\}\{1\}}$. When change features are evaluated in this way, the defect and the environmental change become clearly visible. Each type of upset produces a distinctive *shadow*, which contain *bands*.

The images on the lower row of Figure 35 show *changes* to the $\Delta \boldsymbol{t}$ features which occur as a result of *refining the model mesh and reducing the simulation timestep* (as described in Section 6.1) and *increasing the virtual detector unit size* (as described in Section 6.4)[16]. The changes in $\Delta \boldsymbol{t}$ are very small, relative to the original $\Delta \boldsymbol{t}$ features themselves. The results suggest that the

[15] The defect D3 is a 1 × 1cm^2 defect, and environmental change P1 is a ($\Delta x = \Delta y$ = 1mm) offset in the reference point at which the ply is placed. Refer to Section 6.5 above.

[16] Note: these adjustments are made in *both* of the simulation cases which must be run to produce each change feature image $\Delta \boldsymbol{t}$ that is shown.

model is sufficiently refined that it produces accurate results, and that these results are not strongly impacted by the nominated detector unit size.

Finally, Figure 36 shows the impact that the Type II layup material (uncured visco-elastic epoxy) has upon the change feature images shown in the upper row of Figure 35. While the images appear similar, the component entries in Figure 36 are at least an order of magnitude *smaller* than their equivalent entries shown in Figure 35 (i.e., time delays are much *shorter* than are shown in Figure 35). This reduction occurs despite the fact the Type II material acts as an energy sink (as shown in Figure 31b). A possible reason is that the Type II material is less well acoustically matched to the base plate than the Type I material[17], and therefore, it actually takes disturbances *longer* to penetrate this material.

If Figures 35 and 36 are compared to Figure 20a from Section 5.5 above, it emerges that *Type I material best replicates the response which is observed when a real pre-preg material when laid down on the base plate*[18]. Therefore, a Type I layup material is considered for purpose of analysis which now follows.

Figure 35: Change features, Δt, caused by the Type D3 defect and the Type A1 environmental change (Type I layup material, $\theta = 0.01$).

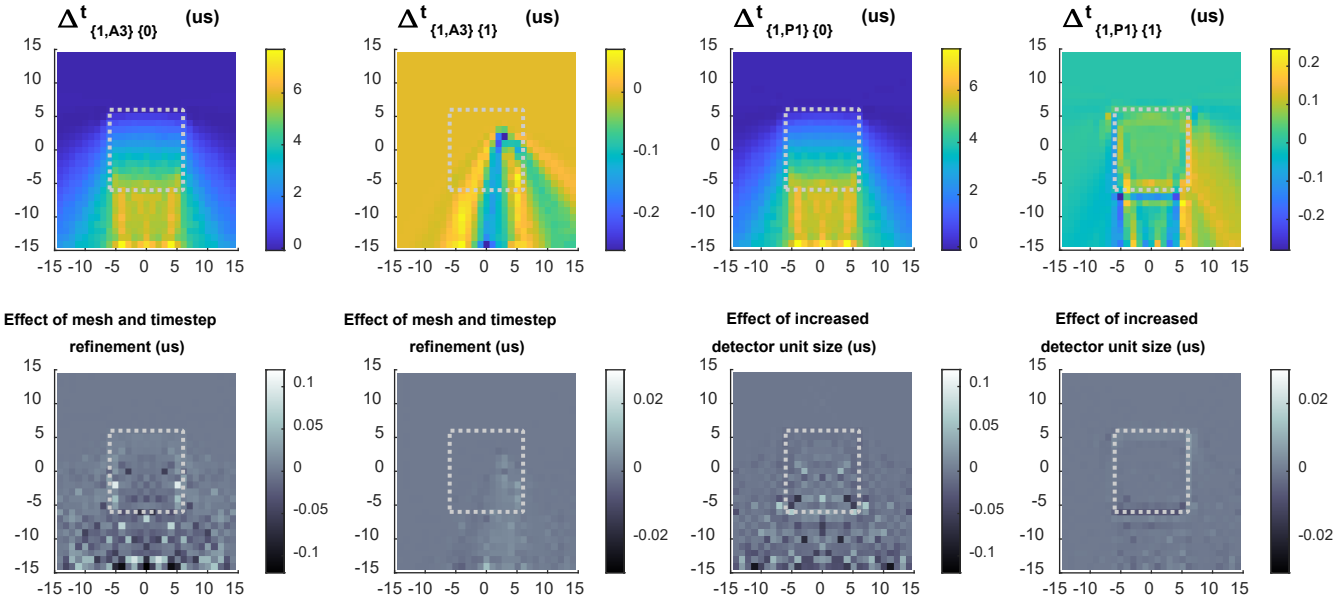

Figure 36: Change features, Δt, caused by the Type D3 defect and the Type A1 environmental change (Type II layup material, $\theta = 0.01$).

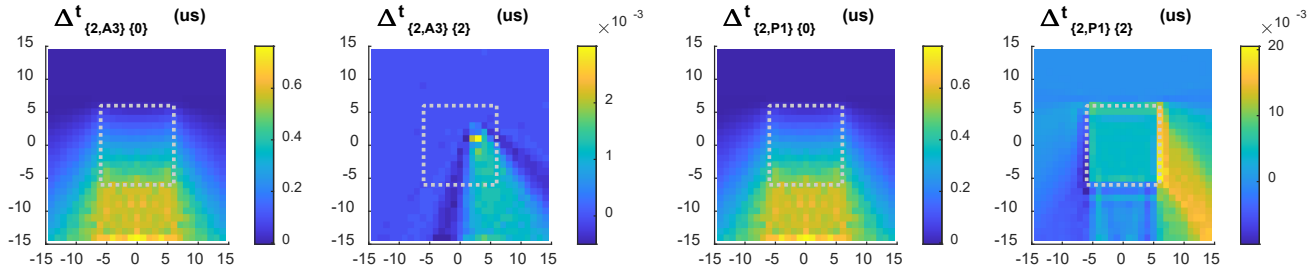

[17] Refer to Table 11. The ratios of layup-material-to-base-plate material Young's moduli and shear moduli are far more extreme for the Type II material than the Type I material.

[18] This comparison is discussed in detail in Section VIII which follows.

7.4 Defect Classification

Figure 37 illustrates the change features $\Delta \boldsymbol{t}_{\{1,a\}\{1\}}$ (where $a \in$ {D1,D2,D3,P1,P2,P3}) which are created when the three types of environmental change and the three types synthetic defect defined in Table 12. These images are produced by simulating Type I layup material, with threshold level parameter $\theta = 0.01$.

The three images to the left of Figure 37 show changes which are caused by introducing the artificial defect types D1, D2 and D3. Each type of defect produces a *distinctive image* which contain 'shadow regions' behind the defect object(s). For defect type D1 (the group of small dispersed defects), these shadow regions merge with one another, while for defects types D2 and D3 (large singular defects), these shadow regions contain bands of alternating polarity which might be attributed to the fact that the defects have *sharp edges*.

The three images to the right of Figure 37 show the changes which are caused by the environmental change types P1, P2, and P3. These images are of particular interest, as they are produced as a result of changes which do not affect integrity of the layup material. Once again, each image is *distinctive*. While the change in ambient temperature (P1) causes a time lag which is, proportional to the actuator-detector separation distance, r, the change in the layup orientation (P2) produces bands, in areas where the carbon fibres and the actuator-detector-pair axes are *closely aligned*[19]. Finally, the shift layup reference point (P3) produces a large 'shadow' regions, wherever the length of material lying between the actuator and any given detector changes significantly.

Figure 38 shows the change features $\Delta \boldsymbol{t}_{\{1,a,b\}\{1\}}$ which are predicted when *two simultaneous changes* are imposed upon the layup materials (i.e. $(a, b) \in \{\mathrm{D1}, \mathrm{D2}, \mathrm{D3}, \mathrm{P1}, \mathrm{P2}, \mathrm{P3}\}$ with the stipulation that $a \neq b$). There are 15 possible permutations of such change features, which are shown above and to the right of the diagonal band in this figure. Each change label *a* is specified in red lettering (labels shown on left of the images) while each change label *b* is specified by blue lettering (labels shown above the images). It may possible to discern that each image is a *mixture* of the single features.

The lower right-hand side of the main diagonal shows the *changes between two sets of difference* features, $\Delta \boldsymbol{t}_{\{1,a,b\}\{1\}} - \Delta \boldsymbol{t}_{\{1,b\}\{1\}}$**.** Again each change label *a* is specified by red lettering (this time, shown on the right of images), while each change label *b* is specified by blue lettering (this time shown below the images). It is evident that images shown in each column are in very good agreement with the images shown in Figure 37 above. This match suggests that the changes which are imposed upon the layup material are *linearly separable*, that is to say that, $\Delta \boldsymbol{t}_{\{1,a,b\}\{1\}} - \Delta \boldsymbol{t}_{\{1,b\}\{1\}} \cong \Delta \boldsymbol{t}_{\{1,a\}\{1\}}$.

Collectively, Figures 37 and 38 indicate that, given a sufficiently dense array of detector transducers, *the defects in the composite material are distinguishable from changes in environmental conditions with a high level of accuracy.*

[19] This result also highlights the fact that the actuator pulse energy propagates more rapidly along the carbon fibres than in the direction normal to the fibres.

Figure 37. Change features $\Delta t_{\{1,a\}\{1\}}$ resulting from a single change to the layup material condition 'a' (θ = 0.01).

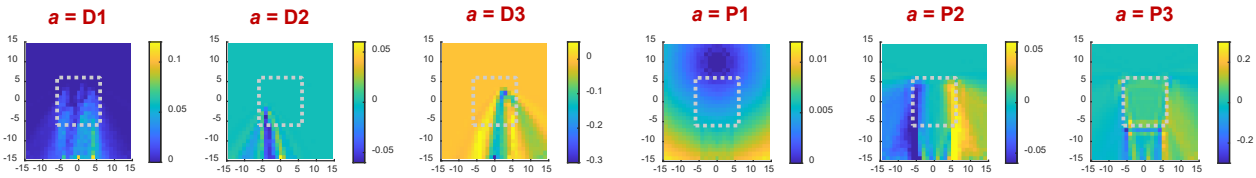

Figure 38: Change features $\Delta t_{\{1,a,b\}\{1\}}$, and differences in change features $\Delta t_{\{1,a,b\}\{1\}}$ - $\Delta t_{\{1,b\}\{1\}}$, resulting from two simultaneous changes to layup material condition 'a' and 'b' (θ = 0.01).

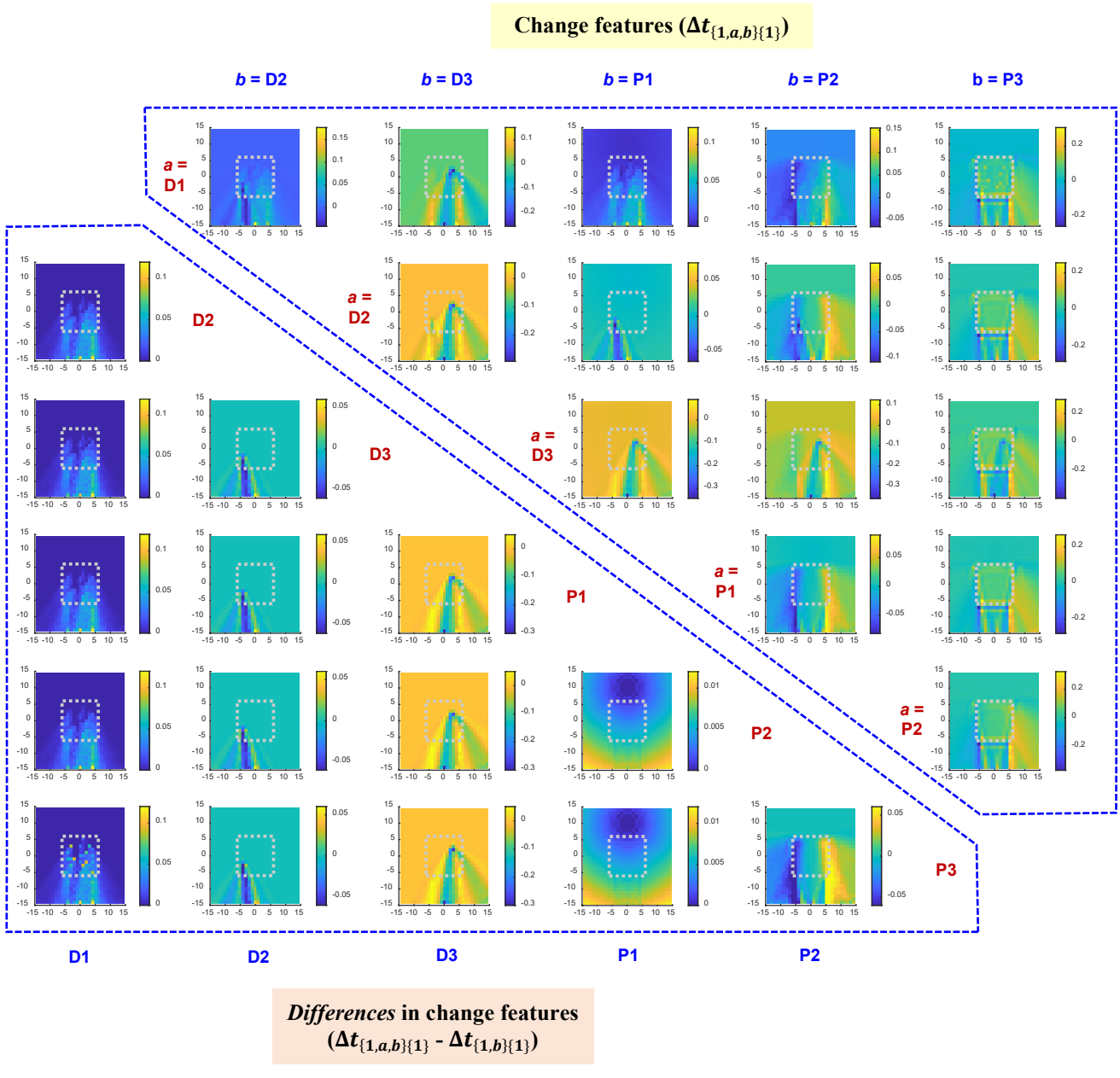

7.5. Summary Statistics

It is convenient to reduce the features shown in Figure 35 to *summary statistics*, as was carried out in Section 5.5, such that the features from experimental benchtests and numerical simulations can be compared.

Table 13 presents summary statistic values, μ, for layup of a single ply layer, and for changes in ambient temperature, ply layup position, and ply orientation (change types P3, P1 and P2 as shown in Table 12). The calculation methods used to derive each statistic, and the indices of the detector features used in each calculation, are shown for reference. The $\bar{\mu}_{a2}$ and $\bar{\mu}_b$ statistics have been are based on mean values, since the ply layup and temperature changes produce features which are of known polarity, while the $\bar{\mu}_{c1}$ and $\bar{\mu}_{c2}$ statistics are based on variances, since these changes produce features which do not have definite polarity. The three detectors which are used to perform each calculation are shown in Figure 19, and are selected in order to be reasonably consistent with the physical benchtests.

As per Table 6, the statistics which are shown on the right-hand side of Table 13 are intended to give crude estimates of changes in the features, t, which could be expected due to the types of changes which are shown.

Table 13: Summary statistics for feature changes caused by *ply layup*, a *change in ambient temperature*, a change in *layup position*, and a change in *layup orientation angle*

Change		Feature	Calculation Method	Averaging Group	Summary Statistic Value
Layup of Single Ply	Transducer pair *parallel* to fibres	$\Delta \boldsymbol{t}_{\{1\}\{0\}}$	$\bar{\mu} = \frac{1}{\lvert S \rvert}\sum \Delta t_n$	n_d = {131}	$\bar{\mu}_{a2}$ = 5834 ns
Change in ambient temperature (1°C)		$\Delta \boldsymbol{t}_{\{1,P3\}\{1\}}$	$\bar{\mu} = \frac{1}{\lvert S \rvert}\sum \Delta t_n$	n_d = {410, 131,432}	$\bar{\mu}_b$ = 6 ns
Change in layup position relative to reference point (Δx = Δy = 1mm)		$\Delta \boldsymbol{t}_{\{1,P1\}\{1\}}$	$\bar{\mu} = \frac{1}{\lvert S \rvert}\sqrt{\sum \Delta t_n^2}$	n_d = {410, 131,432}	$\bar{\mu}_{c1}$ = 41 ns
Change in layup orientation relative to reference angle (2°)		$\Delta \boldsymbol{t}_{\{1,P2\}\{1\}}$	$\bar{\mu} = \frac{1}{\lvert S \rvert}\sqrt{\sum \Delta t_n^2}$	n_d = {410, 131,432}	$\bar{\mu}_{c2}$ = 28 ns

VIII. Comparisons of Summary Statistics

Table 6 (Section 5.6) and Table 13 (Section 7.5) contain summary statistics for the physical benchtests and the numerical simulations. However, these sets of statistics are not directly comparable in their forms shown, since the aluminium base plate materials and layup sheets have *differing dimensions*. To compare the two sets of statistics, it is first necessary to define appropriate *conversion factors*.

8.1 Conversion Factors

Conversion factors, k, which relate numerical simulation output to physical benchtest output are defined in Table 14. These factors are functions of the *base plate area* A_b and the *layup area* A_l in the plane connecting the actuator and detector transducers, as illustrated in Figure 39. As shown, two different conversion formulae applied, depending on which type of change feature is under consideration.

The justification for the conversion factor $k = (A_l/A_b)^B/(A_l/A_b)^S$, which is applied to adjust the summary statistics for the *ply layup*, the *ply offset,* and the *ply orientation*, is straightforward. These changes are expected (to a first approximation) to be proportional to the *relative area* of layup material lying between the actuator and detector as shown in Figure 39. The greater this relative area, the *more energy will be absorbed by the layup material.* As a result, *the greater the change expected in the summary statistic* μ.

The justification for the conversion factor $k = (A_b)^B/(A_b)^S$ which is applied to compare changes due to *temperature variation*, is lengthier, but it is again straightforward. Firstly, it may be assumed that the base plate will expand isotropically due to a small increase in temperature dT. Secondly, it may be assumed that threshold level crossing time features t, are directly proportional to the transducer separation distance r and *inversely* proportional to the S_0 mode velocity c_g^{S0} (i.e., to the fastest-travelling wave group). From the first assumption it follows that the fractional increase in the base area A_b is defined by $dA_b/A_b = \alpha^{2/3}\, dT$, where α is the thermal expansion coefficient for the base material. From the second assumption it follows that $t \cong r/c_g^{S0}$. However, it is also of interest to note that, for the carrier frequency f_c = 280kHz, c_g^{S0} is to a very close approximation inversely proportional to plate thickness t_b[20]. It thus follows that $t \cong c\, r\, t_b$, and hence that $t \cong c\, A_b$ and that $dt \cong c\, dA_b$, where the symbol c is an arbitrary scaling constant. Substituting the expression for dA_b above yields the expression $dt \cong c\, \alpha^{2/3}\, A_b\, dT$; that is to say that *the summary statistic* μ *is proportional to the base plate area and to the change in the ambient temperature.*

Figure 39: Base plate and layup material areas, A_b and A_l

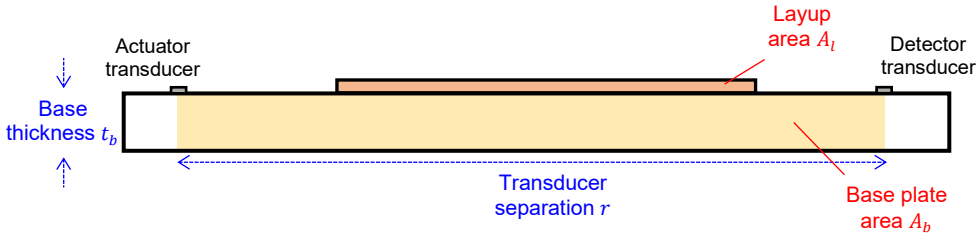

[20] For the t_b = 10 mm and t_b = 4 mm thick base plates used in physical benchtests and in the numerical simulations, the S_0 mode group velocity ratio is c_g^B/c_g^S=1991/5027 = 0.397.

Table 14: Conversion factors k which relate summary statistic μ^B to summary statistic μ^S

Change	Conversion factor k	Calculated k value
Layup of single ply layer	$k_a \sim \frac{(A_l/A_b)^B}{(A_l/A_b)^S}$	0.11
Change in ambient temperature (1°C)	$k_b \sim \frac{(A_b)^B}{(A_b)^S} \cdot \frac{\Delta T^B}{\Delta T^S}$	3.75
Change in layup position relative to reference point ($\Delta x = \Delta y = 1$mm)	$k_{c1} \sim \frac{(A_l/A_b)^B}{(A_l/A_b)^S}$	0.11
Change in layup orientation relative to reference angle (2°)	$k_{c2} \sim \frac{(A_l/A_b)^B}{(A_l/A_b)^S}$	0.11

8.2 Experiment Comparisons

Table 15 presents the summary statistics for physical benchtests μ^B, and the *converted* summary statistics for numerical simulations, $k\mu^S$.

The first row of the Table 15 compares *single ply layup* statistics (for transducer pairs *parallel* to carbon fibres, $k\mu_a^S$ vs. μ_a^B); while the second row compares *temperature change* statistics ($k\mu_b^S$ vs. μ_b^B). These two pairs of statistics are in reasonably close agreement, and would therefore suggest, that the finite element model is physically realistic and can replicate real experimental results.

The third and fourth rows of Table 15 compare the statistics for 'P1' and 'P2' type environmental changes listed Table 6 ('ply offset' and 'ply rotation'), against the *ply placement variation* statistic (i.e. $k\mu_{c1}^S$ vs. μ_c^B and $k\mu_{c2}^S$ vs. μ_c^B). Note that as the underlying cause of the μ_c^B statistic is not known, the comparisons are speculative. The former two statistics are far smaller than the latter, indicating that the changes observed during the physical benchtests *cannot* be explained by these effects; the underlying cause of the difference remains unknown.

Table 15: Summary Statistics Comparison. Converted Statistics for Numerical Simulations vs. Physical Benchtest Statistics.

Imposed Change	Summary Statistic (Numerical Simulations[1])	Converted Statistic (Numerical Simulations)	Summary Statistic (Physical Benchtests[2])
	μ^S	$k\,\mu^S$	μ^B
Layup of single ply layer [3]	5834 ns	648 ns	804 ns
Change in ambient temperature (1°C)	6 ns /°C	22 ns/°C	18 ns/°C
Change in layup position relative to reference point ($\Delta x = \Delta y$ = 1mm)	41 ns	4 ns	223 ns [4]
Change in layup orientation relative to reference angle (2°)	28 ns	3 ns	

Note 1: Values carried forward from Table 12.
Note 2: Values carried forward from Table 6.
Note 3: Values shown are for measurements taken across the layup, parallel to the carbon fibres.
Note 4: Value shown is the summary statistic for the ply placement variation reported in Table 6..

IX. References

Bull, D.J., Helfen, L., Sinclair, I., Spearing, S.M. and Baumbach, T., 2013. A comparison of multi-scale 3D X-ray tomographic inspection techniques for assessing carbon fibre composite impact damage. Composites Science and Technology, 75, pp.55-61.

Feraboli, P., 2009. Composite materials strength determination within the current certification methodology for aircraft structures. *Journal of Aircraft*, *46*(4), pp.1365-1374.

Fuentes, R., Cross, E.J., Ray, N., Dervilis, N., Guo, T. and Worden, K., 2017. In-Process Monitoring of Automated Carbon Fibre Tape Layup Using Ultrasonic Guided Waves. In *Special Topics in Structural Dynamics, Volume 6* (pp. 179-188). Springer, Cham.

Gholizadeh, S., 2016. A review of non-destructive testing methods of composite materials. *Procedia Structural Integrity*, *1*, pp.50-57.

Giurgiutiu, V., 2003, August. Lamb wave generation with piezoelectric wafer active sensors for structural health monitoring. In *Smart Structures and Materials 2003: Smart Structures and Integrated Systems* (Vol. 5056, pp. 111-122). International Society for Optics and Photonics.

Giurgiutiu, V., 2007. *Structural health monitoring: with piezoelectric wafer active sensors*. Elsevier.

Hasiotis, T., Badogiannis, E. and Tsouvalis, N.G., 2011. Application of ultrasonic C-scan techniques for tracing defects in laminated composite materials. *Strojniški vestnik-Journal of Mechanical Engineering*, *57*(3), pp.192-203.

Holmes, C., Drinkwater, B.W. and Wilcox, P.D., 2008. Advanced post-processing for scanned ultrasonic arrays: Application to defect detection and classification in non-destructive evaluation. *Ultrasonics*, *48*(6-7), pp.636-642.

Kim, S., Uprety, B., Mathews, V.J. and Adams, D.O., 2015, March. Numerical simulation and experimental validation of Lamb wave propagation behavior in composite plates. In *AIP Conference Proceedings* (Vol. 1650, No. 1, pp. 1178-1185). American Institute of Physics.

Laflamme, S., Kollosche, M., Connor, J.J. and Kofod, G., 2012. Robust flexible capacitive surface sensor for structural health monitoring applications. *Journal of Engineering Mechanics,* 139(7), pp.879-885.

Lukaszewicz, D.H.A. and Potter, K., 2012. Through-thickness compression response of uncured pre-preg during manufacture by automated layup. *Proceedings of the Institution of Mechanical Engineers, Part B: Journal of Engineering Manufacture*, *226*(2), pp.193-202.

O'Brien, D.J., Mather, P.T. and White, S.R., 2001. Viscoelastic properties of an epoxy resin during cure. *Journal of composite materials*, *35*(10), pp.883-904.

Ochôa, P., Villegas, I.F., Groves, R.M. and Benedictus, R., 2018. Experimental assessment of the influence of welding process parameters on Lamb wave transmission across ultrasonically welded thermoplastic composite joints. *Mechanical Systems and Signal Processing*, *99*, pp.197-218.

Pierce, S.G., Culshaw, B., Philp, W.R., Lecuyer, F. and Farlow, R., 1997. Broadband Lamb wave measurements in aluminium and carbon/glass fibre reinforced composite materials using non-contacting laser generation and detection. *Ultrasonics*, *35*(2), pp.105-114.

Ray, B.C., Hasan, S.T. and Clegg, D.W., 2007. Evaluation of defects in FRP composites by NDT techniques. *Journal of Reinforced Plastics and composites*, *26*(12), pp.1187-1192.

Rokhlin, S.I. and Wang, Y.J., 1991. Analysis of boundary conditions for elastic wave interaction with an interface between two solids. *The Journal of the Acoustical Society of America*, *89*(2), pp.503-515.

Santhanam, S. and Demirli, R., 2013. Reflection of Lamb waves obliquely incident on the free edge of a plate. *Ultrasonics*, *53*(1), pp.271-282.

Lanza di Scalea, F., Rizzo, P. and Marzani, A., 2004. Propagation of ultrasonic guided waves in lap-shear adhesive joints: case of incident A 0 Lamb wave. *The Journal of the Acoustical Society of America*, *115*(1), pp.146-156.

Shen, Y. and Giurgiutiu, V., 2015. Effective non-reflective boundary for Lamb waves: Theory, finite element implementation, and applications. *Wave Motion*, *58*, pp.22-41.

Tallman, T.N., Gungor, S., Wang, K.W. and Bakis, C.E., 2014. Damage detection and conductivity evolution in carbon nanofiber epoxy via electrical impedance tomography. *Smart Materials and Structures*, *23*(4), p.045034.

Ulriksen, M.D., Tcherniak, D., Hansen, L.M., Johansen, R.J., Damkilde, L. and Frøyd, L., 2017. In-situ damage localization for a wind turbine blade through outlier analysis of stochastic dynamic damage location vector-induced stress resultants. *Structural Health Monitoring*, *16*(6), pp.745-761.

Yeum, C.M., Sohn, H. and Ihn, J.B., 2011. Lamb wave mode decomposition using concentric ring and circular piezoelectric transducers. *Wave motion*, *48*(4), pp.358-370.

Zhang, J., Drinkwater, B.W. and Wilcox, P.D., 2008. Defect characterization using an ultrasonic array to measure the scattering coefficient matrix. *IEEE transactions on ultrasonics, ferroelectrics, and frequency control*, *55*(10), pp.2254-2265.

Appendix A: Analytic Solution for Circular-Crested Lamb Waves

The actuation process produces circular-crested type Lamb waves within the base plate. Under such idealised conditions, the wave which would propagate in an infinite base plate can be analytically evaluated. Each frequency component present in the actuation, produces a circular-crested Lamb wave having radial components only, and whose the displacement profile at the upper plate surface $u_r(x,t)_{z=+h}$ is described by the expression (Guirgiutiu, 2007):

$$u_r(r,t)_{z=+h} =$$

$$-\pi i \frac{a\tau_o}{\mu} e^{i\omega t}\left[\sum_{k^s} \underbrace{J_1(k^s a)\frac{N_s(k^s)}{D'_s(k^s)}H_1^{(2)}(k^s r)}_{S\ modes} + \sum_{k^a} \underbrace{J_1(k^a a)\frac{N_a(k^a)}{D'_s(k^a)}H_1^{(2)}(k^a r)}_{A\ modes}\right]$$

where:

$$N_s = kq(k^2+q^2)\cos ph \cos qh$$
$$N_a = kq(k^2+q^2)\sin ph \sin qh$$

$$D'_s(k) = \frac{\partial}{\partial k}\{(k^2-q^2)^2 \cos ph \sin qh + 4k^2 pq \sin ph \cos qh\}$$
$$D'_a(k) = \frac{\partial}{\partial k}\{(k^2-q^2)^2 \sin ph \cos qh + 4k^2 pq \cos ph \sin qh\}$$

$$p^2 = \omega^2/c_L^2 - k^2 \qquad q^2 = \omega^2/c_T^2 - k^2$$

and where h is the plate half-thickness; a is the actuator radius; the k_s and k_a terms are wavenumbers of the S and A modes applicable at each frequency; the J_1 terms are Bessel functions of the first kind, the $H_1^{(2)}$ terms are second Hankel functions of order 1.

Note that the analytic expression given above is strictly only applicable for a base plate having *infinite* dimensions. The reflections of Lamb waves at the boundaries of a finite plate will generate *shear horizontal* wave modes, as outlined by Santhaman & Demirli (2013). These modes absorb energy of the incident Lamb waves, and they render an attempt to obtain an analytic solution impracticable.